Technical Report 1330
February 1990

Frequency Spectrum Characteristics:

Underwater Acoustic Propagation
in Double Ducts

M. Pedersen
D. Gordon
S. Edwards

AD-A221 782

046

NAVAL OCEAN SYSTEMS CENTER
San Diego, California 92152–5000

J. D. FONTANA, CAPT, USN
Commander

R. M. HILLYER
Technical Director

ADMINISTRATIVE INFORMATION

ACKNOWLEDGEMENTS

RT

SUMMARY

OBJECTIVE

The objective of this theoretical report was to perform a detailed examination of the coupling characteristics between two adjacent refractive underwater acoustic ducts. Normal-mode theory was used in this study, with ray theory as an invaluable adjunct.

RESULTS

The characteristics of phase and group velocity and propagation loss were investigated for low-order modes with phase velocities less than the maximum sound speed separating the ducts. Cross-duct and in-duct propagation were evaluated for the source and receiver in different and identical duct(s), respectively. As the frequency was varied, the difference in phase velocity (eigenvalues) between adjacent modes did not have the uniform behavior of single ducts; the phase velocities were pinched together, forming relative minima. These minima formed a set of discrete critical frequencies, with similar spectral characteristics near each critical frequency. The band about each critical frequency displayed a number of interesting characteristics, as follows:

1. Cross-duct propagation has a resonant peak of maximum coupling.

2. In-duct propagation transitions from low to high losses in one duct and vice versa in the other duct.

3. Group velocity transitions between values characteristic of the two single ducts.

4. Points of Airy phase straddle the critical frequency.

5. The standing waves for the adjacent modes strongly resemble each other except for a π phase change for cross-duct source and receiver configurations. This phase change results in a range-periodic exchange (between the ducts) of the energy associated with the adjacent modes.

Detailed numerical examples of these characteristics are presented. The phase-integral method of ray theory provides good first-order approximations to the mode eigenvalues, the critical frequencies, and group velocity.

i

CONTENTS

FIGURES

TABLES

1.0 INTRODUCTION

This report investigates the coupling characteristics between two adjacent refractive underwater acoustic ducts. The authors' first experience with some of the problems posed by double ducts was in a 1969 to 1971 unpublished investigation by Gordon of a surface duct (positive-gradient surface layer) overlaying a near-surface refractive duct. Portions of this investigation, as well as a general discussion of multiple ducts, are published in section 4.3 of reference 1. This investigation demonstrated an enhancement in the cross-duct propagation (source in one duct and receiver in the other duct), when the phase velocities of adjacent normal modes were the same or nearly the same. Two important problems were discovered in the application of a normal-mode propagation model. The first problem involved determining eigenvalues and identifying modes. For a single duct, the eigenvalues fall at semiregular intervals; whereas, for a double duct, they are erratic and not easily predicted. The second problem occurred when the eigenvalues were close for a pair of adjacent modes. Here, the incoherent addition of modes leads to unrealistically small propagation losses; whereas, under most circumstances, the incoherent addition of modes leads to a realistic measure of the dependence of average propagation loss on range.

Difficulty in determining eigenvalues was often encountered by D. White in the normal-mode evaluation of shallow water areas. The analysis of one of these areas was presented in reference 2, while section 5.2.1 of reference 1 presents a brief discussion of the general problems encountered by White. His investigation included two ducts in the water column. The upper duct consisted of surface-reflected propagation in a positive-gradient layer, and the lower duct consisted of bottom-reflected propagation in a negative-gradient layer. This problem was complicated further by a positive-gradient fluid layer used in modeling the sound speed in a sedimentary layer in the subbottom structure. This leads to a third duct in which the sound travels in the sedimentary layer with multiple reflections off the water-sediment interface.

Jensen (reference 3) has also encountered problems with multiple ducts in shallow water. He presents two examples of "channel resonance," which are related to the present study of coupling characteristics. His first example of figure A3 (reference 3) involves two isospeed ducts in the water column, overlaying a bottom of much higher sound speed. His second example of figure 4 (also reference 3) involves a water duct overlaying a positive-gradient, slow bottom, which forms the second duct. Jensen provides experimental data for the second example. He further notes that no strong resonance is apparent in the experimental data because the different bottom layerings along the propagation path break up the regularity.

However, Bucker (reference 4) has used the parabolic equation method to examine the effect of range dependence on the two refractive ducts of this present report. He concludes that moderate range dependence does not destroy the fundamental resonance transfer of energy between ducts, but does cause significant variation in the interchange range. The significance of this conclusion will be indicated in Chapter 4 of this report.

The investigation reported here differs, in one major aspect, from the previously cited, double-duct studies of Gordon, White, and Jensen. These studies involved double-duct configurations with a significant dissipation of energy, resulting in damped modes, i.e., modes with complex eigenvalues. In the examples of White and Jensen, the dissipation process was attenuation in the bottom sediment. In the example of Gordon, dissipation resulted from leakage out of the refractive duct into the deep-water column. In contrast, for the configuration investigated here, the important modes in the coupling process have insignificant damping. For the modes of interest and the critical frequencies, the eigenvalues are essentially real.

This simplifies the problem; for in the case of duct coupling with significant damping, the imaginary part of the eigenvalue is not monotonic with mode number, but can jump about wildly as indicated in figure 33 of reference 1. Moreover, with no significant damping, the coupling effects can be examined at long ranges, because the important modes are not stripped off. Despite this simplification, the present investigation displays many of the features previously encountered for damped modes. The investigation has also revealed some new characteristics which were not apparent in earlier studies. Finally, the sound-speed profile configuration in this report can be modified slightly to introduce significant damping as a subject for further investigation.

This report serves another purpose: it provides test cases for critically evaluating propagation models as discussed at length in reference 1. Many propagation model implementations, which routinely treat single ducts in a satisfactory manner, may encounter severe problems in evaluating the configurations presented here. Reference 5 contains a treatment of the phase-integral method, which plays an important role in the analysis covered in the present report.

This report contains the analysis of mode phase and group velocities, mode amplitude and phase, and propagation loss. Chapter 2 introduces the various constraints used in formulating the cross-duct coupling problem, and Chapter 3 presents theoretical expressions. The major part of this report is Chapter 4, which contains the numerical results for the double duct. Chapter 5 outlines new work on duct coupling.

2.0 PROBLEM FORMULATION

The sound-speed profile of this investigation is presented in figure 2-1 and is based on a profile taken in the North Atlantic. This is a multilayer profile of the form

$$[C_i/C(Z)]^2 = 1 - 2\gamma_i(Z - Z_i)/C_i , \qquad (1)$$

where C_i, γ_i, and Z_i are the sound speed, gradient, and depth at the top of layer i.
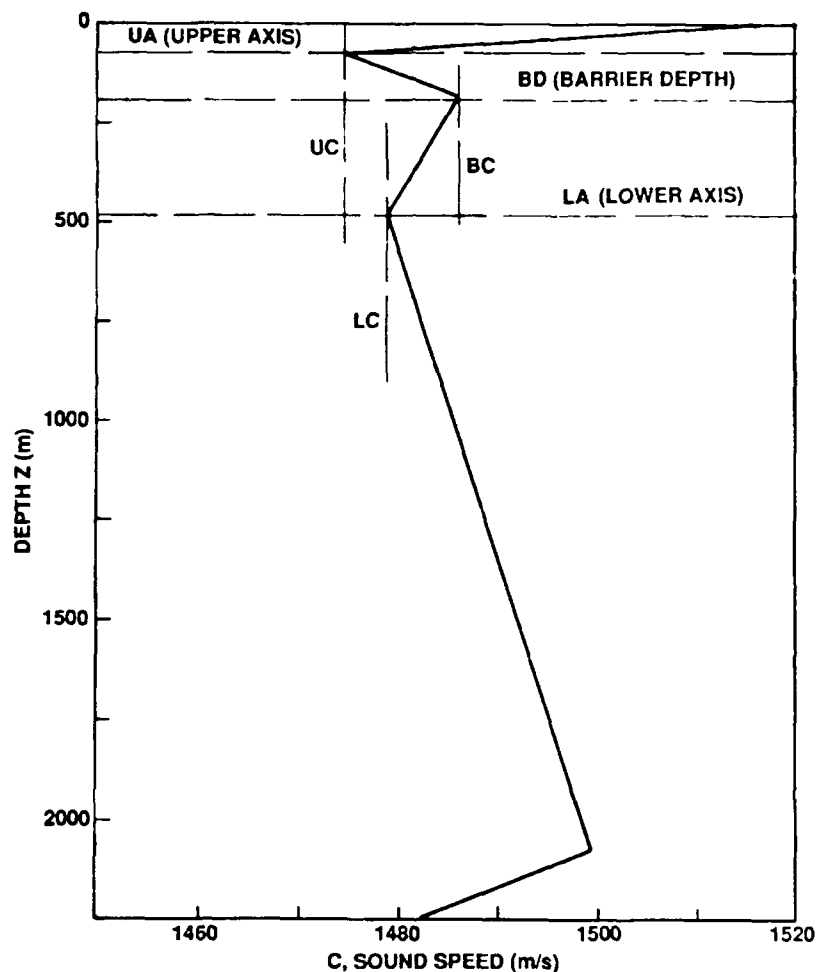
Figure 2-1. The sound-speed profile used in the investigation.

The profile parameters are given in table 2-1, and the parameters Z_i and C_i are exactly as given. The quantity γ_i can be derived from Z_i and C_i and is given here to only five decimal places. Anyone wishing to use these profiles as a control for a normal-mode program should evaluate γ_i to the number of significant digits available with their computer. For example, our normal-mode program uses double precision arithmetic with just over 18 decimal-digits available.

Table 2-1. Parameters for the figure 2-1 profile.

i	$Z_i(m)$	$C_i(m/s)$	$\gamma_i(s^{-1})$
1	0	1516.7	−5.8649
2	76	1474.0	0.11262
3	183	1486.2	−0.02444
4	488	1478.8	0.01265
5	2076	1499.3	−0.10000

The last interface, 2076 m, represents the nominal bottom depth in the area. The profile below this depth consists of a negative-gradient half space with a gradient of −0.1 s^{-1} at 2076 m. This aspect of the model corresponds to a lossy bottom and will be discussed further in the next chapter.

The profile consists of two refractive ducts with the axis of the upper duct at 76 m and of the lower duct at 488 m. These are designated in figure 2-1 as UA and LA, respectively. The barrier depth of 183 m is designated as BD.

The sound speeds corresponding to these three critical depths are designated respectively as UC, LC, and BC. These same letters for the three critical depths or sound speeds will be used in other figures which follow. The axial sound speed of the upper duct is 4.8 m/s less than that of the lower duct, and the sound speed at the barrier depth is 7.4 m/s larger than that at the axis of the lower duct.

The purpose of our formulation is to maximize the cross-duct propagation in the context of barrier penetration. This places certain constraints on the problem. The source and receiver depth must be located in different ducts, and the sound speed at the source and receiver must not exceed the barrier sound speed. As a matter of convenience, we will consider the source to be located in the upper duct and the receiver in the lower duct. (Because of reciprocity, the propagation loss would be the same for a source in the lower duct and a receiver in the upper duct.) Hence, the source depth is constrained between the barrier depth and its upper conjugate and the receiver depth between the barrier depth and its lower conjugate. For the profile of figure 2-1, the source depth is constrained between 53.6 and 183 m, and the receiver depth between 183 and 1068.8 m. A further constraint is that the modes for which the propagation is to be maximized must be modes with phase velocities less than the barrier sound speed.

The purpose of these constraints can be viewed from a ray-theory standpoint. The discussion is facilitated by figure 2-2, which is a ray diagram for a source located in the upper duct at a depth of 82.744 m. Two rays are shown propagating in the upper duct. These rays have phase velocities which are slightly less than the barrier sound speed. The ray paths, corresponding to the constrained modes, all have phase velocities less than these two rays; and all will be confined to the upper duct. They will not reach a receiver in the lower duct, at least in the sense of the conventional ray diagram of figure 2-2. Our purpose is to determine frequency, and source and receiver depths, to transfer maximum acoustic energy via the constrained modes. This is a wave-theory phenomenon, known as barrier penetration.
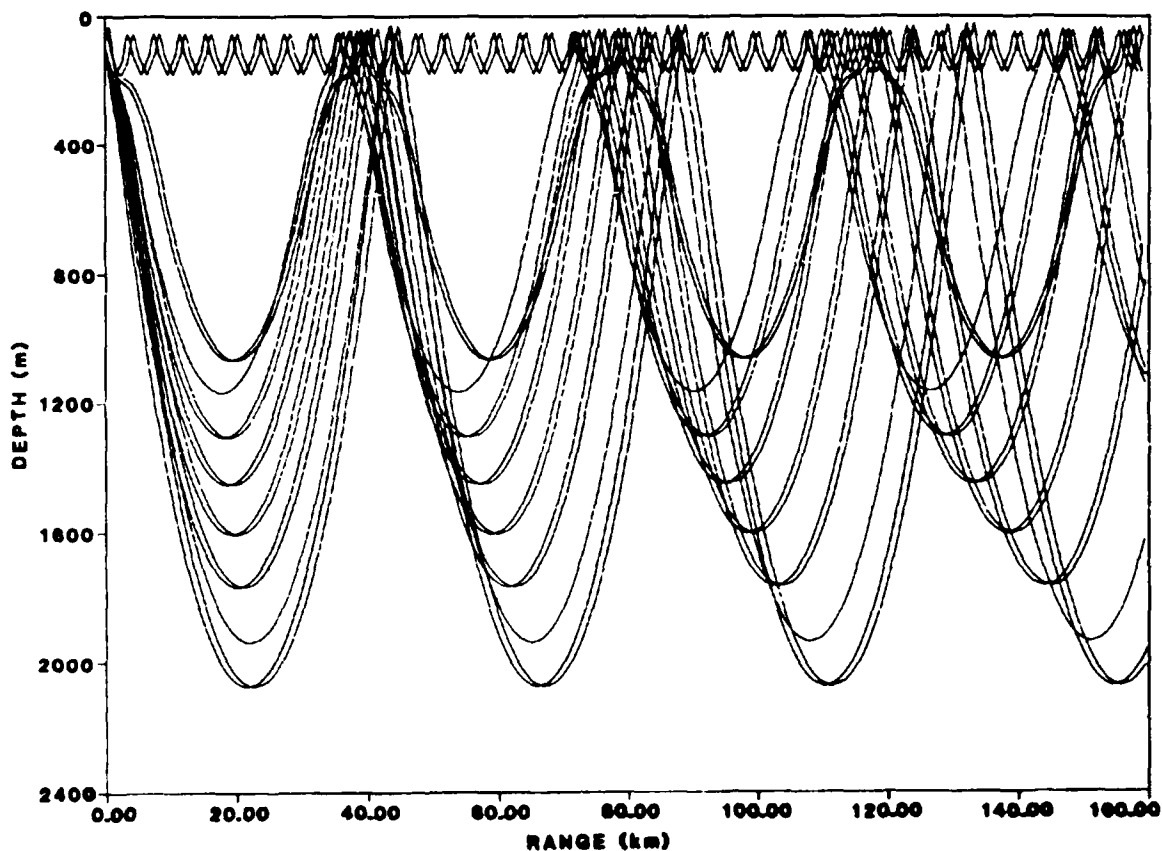
Figure 2-2. Ray diagram for a source depth of 82.74 m.

Figure 2-2 also shows a set of steeper-angle rays, which are selected to illustrate the convergence-zone propagation for the profile of figure 2-1. The ray of smallest angle of this set has a phase velocity which is slightly greater than the barrier sound speed. The ray of largest angle grazes the ocean bottom at a depth of 2076 m at a sound speed of 1499.3 m/s. Since this sound speed is less than that at the ocean surface, no surface-reflected rays are in figure 2-2. All convergence-zone rays form an apex in the negative-gradient layer of the upper duct and a nadir in the positive-gradient layer of the lower duct.

In this report, convergence-zone propagation is of minor interest. However, since it contributes to the total acoustic field, this propagation represents a complication to be dealt with. Figure 2-2 will be useful later in explaining some of the numerical results of Chapter 4.

5

3.0 THEORY

The velocity potential of mode theory may be written as

$$\psi(r, Z) = - i\pi \, e^{i\omega t} \sum_{n=1}^{\infty} H_o^{(2)}(\lambda_n r) U_n(Z, Z_s) \ , \tag{2}$$

where

$$U_n(Z, Z_s) \cong U_n(Z) U_n(Z_s)/D_n \ . \tag{3}$$

Here, r is the range, Z is the receiver depth, Z_s is the source depth, λ_n is the eigenvalue for mode n, $U_n(Z)$ and $U_n(Z_s)$ are the receiver and source depth functions (satisfying a Helmholtz equation), and D_n is the mode normalization factor. The propagation loss associated with equation (3) may be written as

$$H = - 20 \log |\psi| + 10 \, \log \, [C(Z)/C(Z_s)] \ . \tag{4}$$

All of the details, such as the form of $U_n(Z)$ and how to determine λ_n and D_n, are given in reference 6.

In this formulation, the eigenvalues are complex. Several quantities of physical interest, related to λ_n, may be derived from the first term of the asymptotic expansion of the Hankel function in equation (2). The first quantity is the mode-phase velocity, given by

$$C_{pn} = \omega/Re\lambda_n \ . \tag{5}$$

The second quantity is the mode attenuation coefficient, given by

$$a_n = - 8.686 \, Im\lambda_n \ . \tag{6}$$

The dimensions of C_{pn} and a_n are in m/s and dB/m, respectively.

For our purposes here, the second term in equation (4) is not significant and will be suppressed for the remainder of this report. Thus, we define the propagation loss associated with an individual mode as

$$H_n = - 20 \, \log \, |\psi_n| \ . \tag{7}$$

where ψ_n is the evaluation of equation (2) for mode n. With the use of the first term of the asymptotic expansion of $H_o^{(2)}(\lambda_n r)$, we may write

$$H_n = H_{no} + 10 \log r + \lambda_n r \ . \tag{8}$$

Here

$$H_{no} = - 20 \log |U_n(Z, Z_s)| + 10 \, \log |\lambda_n| - 7.98 \ . \tag{9}$$

In this study, we ignore the attenuation due to absorption in the water. The attenuation of equation (8) arises from mode leakage; and in the case of the profile of figure 2-1, from energy leaking down into the half space.

We used a negative-gradient half space in this investigation to simplify the problem and also because we were not concerned with bottom-reflected propagation. Use of a more realistic bottom can

7

lead to additional ducts in the bottom sediment as discussed in the introduction. One advantage to the negative-gradient half space is circumventing the contribution of the branch-line integral (reference 7). A disadvantage is that the slope discontinuity at the top of the half space introduces reflections from the interface. For example, in the study of reference 8, these reflections were apparent in the normal-mode results in the ray-theory shadow zones and had to be suppressed by complicating the sound-speed model. However, neither the above-cited advantage or disadvantage is important in this investigation.

What is important is the fact that the sound speed at the ocean bottom is about 13 m/s larger than the barrier sound speed, which means that the modes of greatest interest have no significant attenuation. In this case, H_{no} of equation (9) is a satisfactory measure of mode strength.

Thus far, our treatment applies to normal-mode theory in general. We now define some expressions, which will be particularly useful in analyzing the coupling between double ducts. Consider

$$U_{nM} = MAX |U_n(Z, Z_s)| .$$ (10)

In equation (10), the source and receiver depths are placed at the strongest antinode in the upper and lower duct respectively. This procedure maximizes $|U_n(Z, Z_s)|$ as a function of source and receiver depth.

Corresponding to equation (9), we may define

$$H_{noM} = - 20 \log |U_{nM}| + 10 \log |\lambda_n| - 7.98 .$$ (11)

Here, H_{noM} represents a quantitative measure of the maximum coupling between ducts for mode n. One of the chief procedures of this article is to investigate the dependence of H_{noM} on frequency, i.e., to determine frequencies of maximum coupling between ducts. The definitions of equations (10) and (11) will be made clearer when the numerical results in the Propagation Loss paragraph in Chapter 4 are presented.

Now, as will be shown later, maximum coupling between ducts occurs near the frequencies where two adjacent modes have almost the same eigenvalues. This introduces an additional complication because the phase relationship between the two modes, n and $n+1$, plays a significant role. The phase of mode n at range r may be written as

$$P_n = \arg \{U_n(Z, Z_s)\} + \arg \{\lambda_n^{-1/2}\} - r \, Re\lambda_n + \pi/4 .$$ (12)

Now we may suppress the second term in equation (12) because $Re\lambda_n \gg Im_n$. The difference in mode phase may be written as

$$P_{n+1} - P_n = \Delta P_{n+1} + r \, 2\pi/R_{n+1} ,$$ (13)

where

$$\Delta P_{n+1} = \arg \{U_{n+1}(Z, Z_s)\} - \arg \{U_n(Z, Z_s)\}$$ (14)

and

$$R_{n+1} = 2 \, \pi(Re\lambda_n - Re\lambda_{n+1})^{-1} .$$ (15)

Equation (15) is a familiar expression for the interference distance between adjacent modes. For example, on page 103 of reference 9, it is referred to as mode-interference wavelength. Equation (14)

8

can be regarded as the phase difference at zero range. As will be shown later in the paragraph, Example of Extremely Close Coupling, in Chapter 4, ΔP_{n+1} is typically zero or $\pm\pi$.

We will now consider four situations. If $\Delta P_{n+1} = 0$, then modes $n+1$ and n are exactly in phase when

$$r = \ell R_{n+1} \tag{16}$$

and are exactly out of phase when

$$r = (\ell + 1/2)\ R_{n+1}\ , \tag{17}$$

where ℓ takes on integral values. Conversely, if $\Delta P_{n+1} = \pm\ \pi$, then the modes are in phase at the ranges of equation (17) and out of phase at the ranges of equation (16). The previously referenced paragraph, Example of Extremely Close Coupling, will present examples of these four situations.

With the use of equation (5), equation (15) may be written as

$$R_{n+1} = f^{-1} C_{pn}\ C_{p,n+1}/(C_{p,n+1} - C_{pn})\ . \tag{18}$$

For single ducts, the phase velocities of adjacent modes are well separated. Here, R_{n+1} corresponds to the loop length of a ray with phase velocity midway between that of the two modes. Agreement between mode theory and ray theory is quite good.

However, in the case of multiple ducts, the phase-velocity differences between adjacent modes can be quite small. These lead to extremely large values of R_{n+1}. An example will be given in the next chapter, in the paragraph on extremely close coupling. (In the case of damped modes, the phase velocity of adjacent modes can be equal, which leads to an infinite ratio for equation (18).) Large values of R_{n+1} cannot be obtained from simple geometric ray theory, and the scope of this report precludes investigating a modified ray theory which can produce such large values. As we shall see, the denominator of equation (18) is strongly frequency dependent. Consequently, any modified ray theory must contain this strong dependence.

4.0 NUMERICAL EXAMPLES

This is the major chapter of this report. It presents all of the numerical results and develops additional theoretical expressions as necessary. The paragraph on phase velocity treats the phase velocity of both ray and mode theory; and the next paragraph, Propagation Loss, mainly concerns optimizing the propagation for a source in the upper duct and receiver in the lower duct. A case of extremely close coupling between modes 1 and 2 is examined in the subsequent paragraph, Example of Extremely Close Coupling. The next paragraph presents the analysis of propagation for both source and receiver in the same duct, after which the group velocity of mode theory is compared with that of ray theory. Before presenting the discussion on the phase velocity of both ray and mode theory, we outline how the various normal mode results are obtained as a function of frequency.

The computer program described in reference 10 generates the numerical examples of this report. Part of this program is called the mode-follower program and is indispensable for analyzing double ducts. This program traces the eigenvalue for a given mode number as some parameter is varied. In this report, the parameter is frequency; however, page 308 of reference 11 illustrates an example where the quantity varied is a dimensionless mathematical parameter. Pages 103 and 104 of reference 2 illustrate another example where the quantity is a profile parameter.

The advantage of this program is that the eigenvalues for a given mode number are continuous functions of frequency. At fixed frequencies, the eigenvalues are discrete points, which can be very difficult to interpret. The continuous curves generated by the mode-follower program clarify the behavior at fixed frequencies. Moreover, this program can be used to determine the critical frequencies of coupling between double ducts.

The standard outputs of this program are mode-phase velocity, mode attenuation, and mode-group velocity as a function of frequency. The program has been modified slightly for this investigation. One modification is a fixed-step interval, rather than a computer-determined interval, when needing to compare results for two different modes at the same set of frequencies. A second modification involves evaluating the cross-duct coupling function of equation (11), which will be described in more detail later.

PHASE VELOCITY

We now apply the phase-integral approximations of reference 5 to the profile of figure 2-1. Figure 4-1 presents the phase velocity as a function of frequency. Consider first the curves of ray theory. The dashed curves are plots of equation (87) of reference 5 for the first nine values of n, evaluated for the axial parameters of the upper duct. The solid curves are the counterparts for the axial parameters of the lower duct. Here, for a given frequency, the phase velocity increases with mode number. Thus, for each set of curves, the lowest curve is for $n=1$, while the highest curve is for $n=9$.

For a given mode number, the phase velocity decreases with increasing frequency. The interface sound speeds are represented in figure 4-1 by the horizontal lines, which are designated as in figure 2-1. We see that the curves approach the axial sound speed, C_a, as a limit as $f \to \infty$. Consequently, the solid curves of figure 4-1 appear asymptotic to LC, while the dashed curves would be asymptotic to UC, if the curves are extended to higher frequencies. These results also follow directly from equation (87) of reference 5.

11
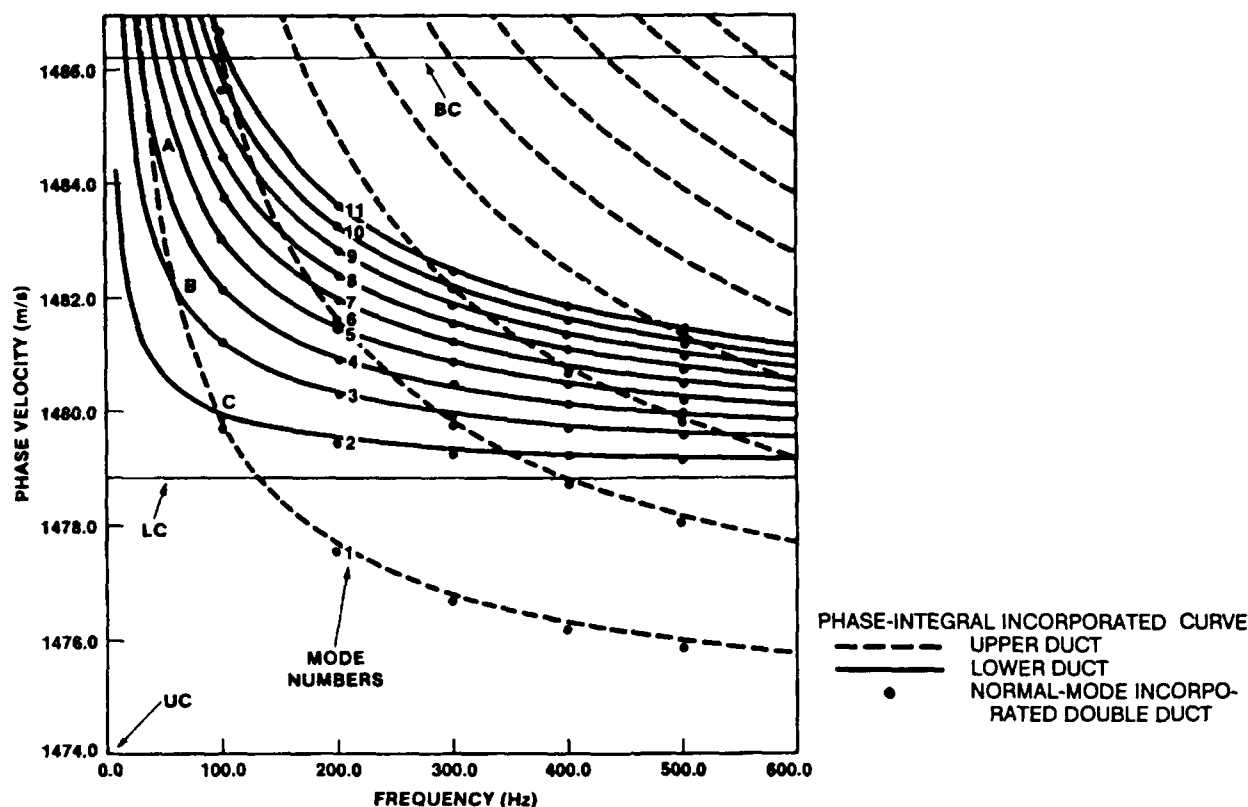
Figure 4-1. Phase velocity as a function of frequency. The curves are ray-theory approximations for single ducts. The dots represent normal-mode evaluations for the double duct.

The curves are extended beyond the barrier sound speed, BC, but no longer apply in this region. Remember that the two sets of curves in figure 4-1 treat the individual ducts and do not represent the double-duct configuration. The results have no meaning for phase velocities above BC, because the upper duct does not extend below BC, and the lower duct does not extend above BD. For phase velocities between BC and C5 of table 2-1, the rays traverse both ducts. These are the convergence zone rays of figure 2-2.

Now, the normal-mode results are considered. The dots in figure 4-1 represent the result of equation (5), as evaluated by normal-mode theory for the double-duct profile of table 2-1. They are shown here at integral multiples of 100 Hz. Significant agreement exists between the normal-mode values for the double duct and the phase-integral values for the individual ducts.

For the single-duct case, the n of equation (89) of reference 5 represents the mode number. However, in our application to double ducts, this n represents the number of the mode for the single duct rather than the mode number for the double-duct configuration. Thus, our next task is to address the problem of mode number.

Now the modes of the double duct are ordered by increasing phase velocity. In figure 4-1, consider the frequency of 200 Hz, where we have numbered the modes to the right of the dots. The first mode corresponds to the $n=1$ curve for the upper duct. The second through fifth modes correspond respectively to the $n=1$ to four curves for the lower duct. The sixth mode corresponds to the $n=2$ curve for the lower duct. The seventh through eleventh modes correspond respectively to the $n=5$ to nine curves for the lower duct.

12

The phase-integral result does more than just approximate the eigenvalues. It also tells us which duct the mode belongs to, even in the context of double ducts. Consider, for example, modes 6 and 7 at 200 Hz. Mode 6 lies close to the dashed line for $n=2$ and belongs to the upper duct; whereas, mode 7 on the solid line number 5 belongs to the lower duct.

Figure 4-2 illustrates the meaning of the term "belonging to the upper duct" by presenting the depth function of equation (3), expressed on a dB scale, for receiver depths from 0 to 1000 m. The mode number is 6. The source depth is 120 m and is located near the maximum response in the upper duct. The barrier depth, BD, separates the upper duct from the lower duct. The first node of any depth function is always at the surface, since this is one of the boundary conditions.

Observe that this mode has the proper number of six nodes and six antinodes. Two of the antinodes are strong in the upper duct, while the remaining four antinodes in the lower duct correspond to a propagation loss which is more than 80 dB greater. The key feature is that the phase-integral result for the upper duct for $n=2$ corresponds to two strong antinodes in the upper duct.

Figure 4-3 is the counterpart of figure 4-2, but for mode 7, where the source depth is in the lower duct at 390 m. Five strong antinodes in the lower duct correspond to $n=5$ for the phase-integral result for the lower duct. In this case, the response for the two antinodes in the upper duct has about 80-dB greater loss than for those in the lower duct. Thus, the number n in the phase-integral method for one of the ducts tells us how many strong antinodes the corresponding double-duct mode has in that particular duct.

Figure 4-3, here, and the previous figure 4-2, are good examples of miniscule barrier penetration. The key to substantial penetration and coupling between the ducts is the region where the phase-integral curves cross each other.

Return now to figure 4-1. Note that curve 1 for the upper duct crosses curves 1 to 3 for the lower duct in three places labeled A, B, and C. For reasons discussed later, we will concentrate on crossing B, for which the phase velocity is about halfway between the sound speed of the lower axis and the barrier.

Figure 4-4 presents a blowup of crossing B. The solid curve is the phase-integral result for mode 2 of the lower duct, and the dashed curve is the phase-integral result for mode 1 of the upper duct. Circles represent the normal-mode phase velocities, which were evaluated at 0.5-Hz intervals from 40.5 to 72 Hz. The lower and upper set of circles are for modes 2 and 3, respectively, of the double duct.

A typical example of eigenvalue behavior is shown here, which we have observed in various double-duct configurations. The modal eigenvalues do not cross each other as predicted by the phase-integral approximation. They veer away from each other, forming a point of closest approach. The frequency of closest approach is 54.43 Hz, and the difference in phase velocity is 0.17259 m/s.

Observe in figure 4-1 that the modal values consistently lie below the phase-integral curves for modes 1 and 2 of the upper duct. Similarly, in figure 4-4, the phase-integral result for mode 1 of the upper duct lies significantly above the normal-mode counterparts. In studying the normal-mode solution for single unbounded ducts, we found that most of the discrepancies just cited occurred because the phase-integral solutions only approximate the mode-theory result for single unbounded ducts. This study is discussed in reference 5. Figure 9 of reference 5 compares the phase-integral results to the mode results for the single-duct formulation of the profile of figure 2-1.
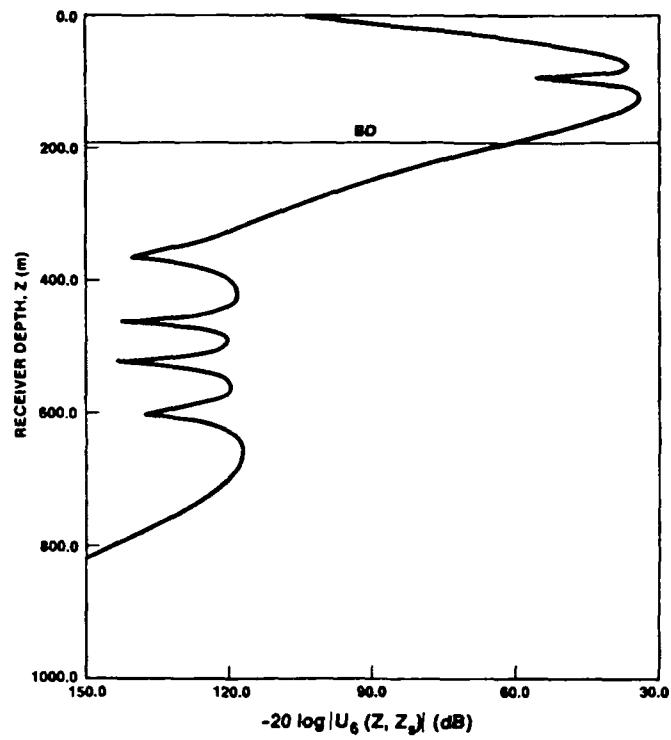
Figure 4-2. The depth function for mode 6 at 200 Hz.
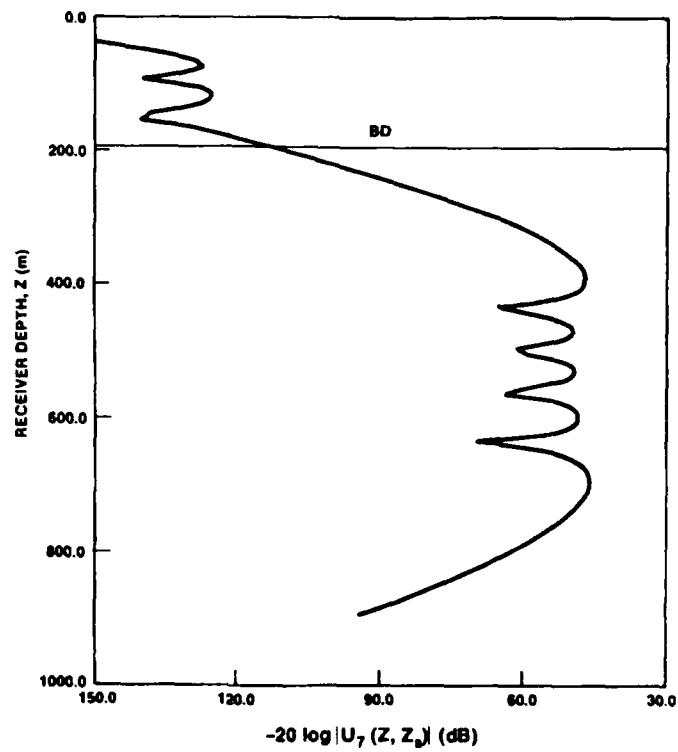
Figure 4-3. Counterpart of figure 4-2 for mode 7.

14
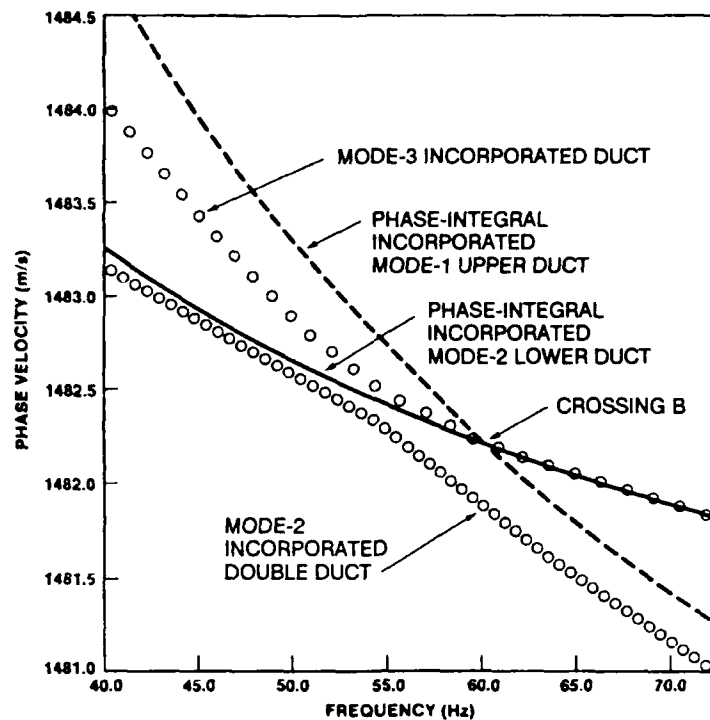
Figure 4-4. The region at point B of figure 4-1 on an expanded scale.

Reference 5 presents a modified phase-integral approach in which the results are completely congruent to the normal-mode results for an unbounded refractive duct. Figure 10 of reference 5 compares the results of this modified approach with the normal-mode values of figure 4-4. The modified approach shows significant improvement over the comparison of figure 4-4. Thus, the modified phase-integral curves will yield very good approximations to the phase velocities of a double duct, except in the area around the intersection of the modified phase-integral curves.

PROPAGATION LOSS

The first step in analyzing propagation loss is to determine the frequencies of maximum coupling between ducts. Figure 4-5 presents the cross-duct coupling function of equation (11) from 20 to 90 Hz for modes 2 to 8. Before discussing the details of figure 4-5, we outline how the curves are generated by the mode-follower program, which follows along a given mode number.

First, we describe the initialization procedure. The eigenvalue is found for the given mode number at some convenient starting frequency. Then, the eigenfunctions are plotted; and the depths of various antinodes are determined. Depths of certain antinodes are selected to form a set of critical depths. This set may be all antinodes for small mode numbers; but for large mode numbers, the set will be pared to the most important antinodes, i.e., ones associated with the smaller losses. One of these critical depths is designated as source depth, which is the depth corresponding to the strongest antinode in the upper duct.

15
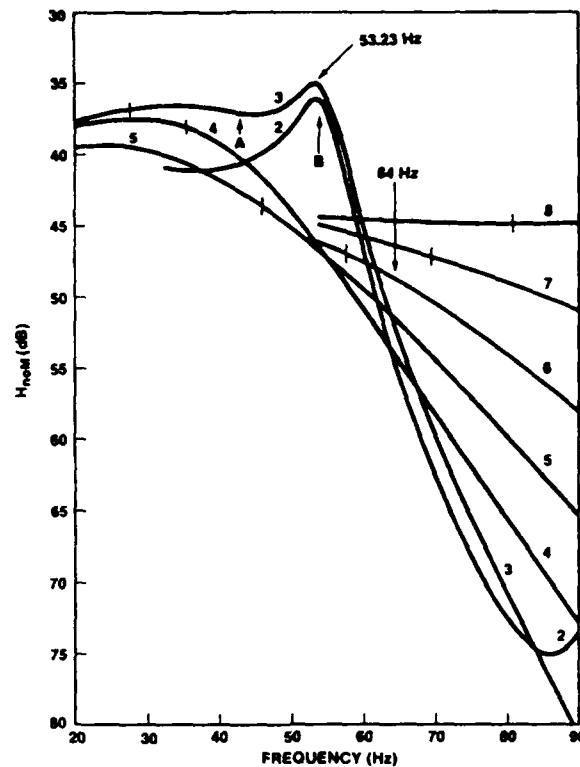
Figure 4-5. Cross-duct coupling function
from 20 to 90 Hz for modes 2 to 8.

The mode-follower program then proceeds to advance this information to a new frequency by
stepping up or down in frequency, as desired. After stepping to a new frequency, the program first
determines the eigenvalue. It then evaluates the new source depth and the new value for $U_n(Z_s)$ of
equation (3). This is done by fitting a parabolic section to evaluations of $U_n(Z)$ at three evenly spaced
depths. The center one of these three depths is taken to be the source depth for the previous fre-
quency. The peak of this parabola then gives the value of $U_n(Z_s)$, and the location of the peak gives
the new source depth. This same parabolic-fitting procedure is then applied to each of the set of criti-
cal depths to obtain the new values of critical depth and their associated depth function $U_n(Z)$. Equa-
tion (3) is next evaluated for the source depth and each of the critical depths, which are taken to be
receiver depths. Equation (9) is then evaluated for each receiver depth with the results printed out.
The smallest value of H_{no} for critical depths in the lower duct is the desired result, i.e., the H_{noM} of
equation (11). The follower program subsequently steps to a new frequency, and the process is
repeated.

Now refer to the details of figure 4-5. The short vertical bars which cross the curves designate the
frequency for which the phase velocity of that mode equals the barrier sound speed. Thus, for fre-
quencies to the left of the bar, no barrier penetration (in our context) exists.

The most significant feature is the resonant peak for mode 3 and for mode 2. The minimum
value of H_{noM} for mode 3 occurs at a frequency of 53.23 Hz for a source depth of 101.844 m and a
receiver depth of 678.325 m. The minimum value of H_{noM} is 35.0167 dB. Corresponding values for
mode 2 are 53.40 Hz, 103.00 m, 664.24 m, and 36.0344 dB. The frequency of closest approach in
figure 4-4 is 54.43 Hz, which is labeled by the letter B in figure 4-5. Hence, the minimum value of
H_{noM} for mode 3 and 2 lies at 1.20 and 1.03 Hz, respectively, less than letter B. Note that both the

16

first and second terms of the right side of equation (11) depend on frequency. Consequently, the frequency which maximizes equation (11) will not be quite the same as that which maximizes equation (10). The dependence of λ_n on frequency is as f. A decrease in frequency decreases the contribution of the second term in equation (11). This explains why the minimum value of H_{noM} lies at a slightly smaller frequency than the frequency of closest approach of the eigenvalues.

The resonant peaks are not excessively sharp. The Q for the second mode peak is 6.7. We cannot give the Q for the third mode because the response does not drop 3 dB on the low frequency side. However, the width at the 1- and 2-dB down points are 4.4 and 8.4 Hz, respectively.

The frequency of closest approach for modes 3 and 4 has been determined to be 42.70 Hz and is labeled here by the letter A. However, the resonance phenomenon does not appear here. The reason will be discussed later on in this chapter in the paragraph entitled, Example of Extremely Close Coupling, which also addresses crossing C of figure 4-1.

We chose 53.23 Hz as our critical frequency for investigation in this section because this frequency has the smallest value of H_{noM} in figure 4-5. In this investigation, we wish to compare the cross-duct propagation loss at 53.23 Hz with that of a second nonresonant frequency, choosing 64 Hz as this second frequency. In figure 4-5, we see that of the modes with a phase velocity less than the barrier, mode 6 has the maximum cross-duct response. The cross-duct response of this mode at 64 Hz has about 13 dB-more loss than the mode 3 response at 53.23 Hz. Consequently, we would predict a substantial difference between these frequencies.

Figure 4-6 presents the depth functions at the critical frequency, with the solid and dashed curves referring to modes 3 and 2, respectively. The source depth is at the first antinode of mode 3 at a depth of 101.844 m. Contrast the depth functions of figures 4-2 and 4-3 to those of figure 4-6, in which the antinodes in the upper and lower duct are of comparable amplitude. This illustrates the significance of duct coupling. Note that mode 2 strongly resembles mode 3, because the eigenvalues are relatively close to each other. Both mode 3 and mode 2 appear to have three antinodes or peak responses.

The step functions in figure 4-6 represent arg $\{U_n(Z, Z_s)\}$, i.e., the phase angle of the depth functions. These functions jump back and forth between π and zero and establish the fundamental difference between modes 2 and 3. The number of phase jumps is one less than the mode number. The solid step function for mode 3 jumps from π to zero at the second node. It jumps back from zero to π at the third node. The dashed step function for mode 2 jumps from π to zero at the second node. Observe that mode 2 endeavors to look like mode 3 by forming an extra peak and valley. However, the extra valley is not accompanied by a jump in phase and does not represent a node. Consequently, it does not count in establishing the mode number.

The relationship between the phase of modes 2 and 3 plays an important role in the propagation characteristics. In order to explain these characteristics, the coherent addition of modes 2 and 3 must be considered. The coherent propagation loss of adjacent modes may be written as

$$H_c = H_{n+1,0} + 10 \log r - 10 \log M_o ,$$ (19)

where

$$M_o = 1 + \beta^2 + 2\beta \cos(P_{n+1} - P_n)$$ (20)

and

$$\beta = (C_{pn}/C_{p,n-1})^{1/2} |U_n(Z, Z_s)| / |U_{n+1}(Z, Z_s)| .$$ (21)

Equation (19) is closely related to equation (4.20) of reference 9. One factors out the larger pressure of equation (4.20) and converts to propagation loss.
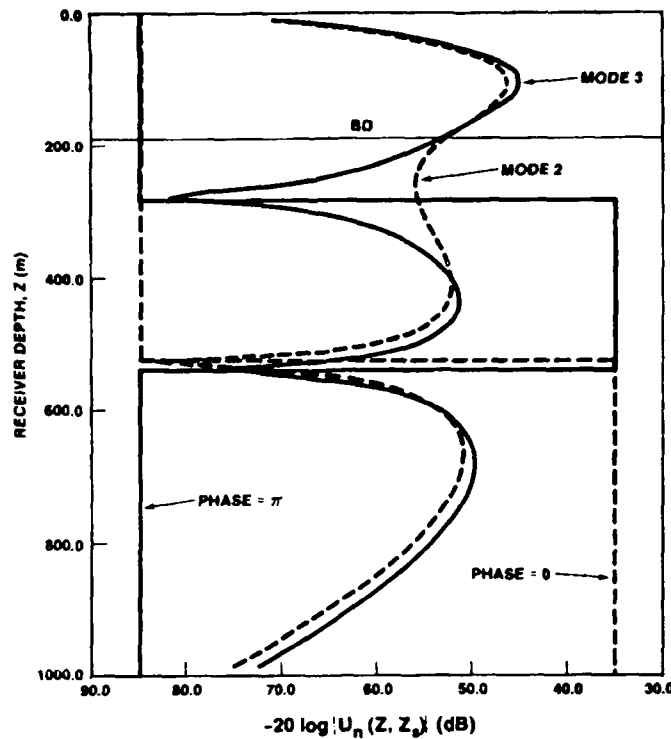
Figure 4-6. Depth function at 53.23 Hz for modes
2 and 3. The step functions represent the phase of
the depth function.

The importance of phase is best illustrated by the two different configurations of table 4-1. Consider first the cross-duct configuration. Here, the source depth is at the first antinode of mode 3 in figure 4-6, and the receiver depth is at the third antinode of mode 3. The interference distance is 223.8 km as given by equation (18). The value of H_{30} is the smallest value of H_{noM} in figure 4-5. The value of β is less than one and can be associated in figure 4-6 with the larger loss for mode 2 at 679.32 m, as compared to mode 3. The value of ΔP_3 of equation (14) is π, which is the difference between the phase of mode 3 and mode 2 at 679.32 m in figure 4-6.

Table 4-1. Parameters of equation (19) for cross-duct and in-duct configurations at 53.23 Hz.

	Cross-duct Configuration	In-duct Configuration
SOURCE DEPTH (m)	101.844	101.844
RECEIVER DEPTH (m)	679.320	101.844
INTERFERENCE DISTANCE (km)	223.8	223.8
H_{30} dB	35.0	30.7
β	0.879	0.866
P_3 (radians)	π	0

18

The in-duct configuration differs in several respects from the cross-duct configuration, with the receiver located in the upper duct at the source depth. The value of H_{30} is 4.3 dB less for the in-duct case. This difference is associated with the difference in figure 4-6 between the mode-3 amplitude at the third antinode and at the first antinode. Note, in passing, that 53.23 Hz does not represent an optimum frequency for the in-duct configuration. This will be addressed in more detail later in this report. The value of β is comparable to that of the cross-duct case. This corresponds to the fact that in figure 4-6, the difference between the solid and dashed curves is about the same at the first antinode as it is at the third antinode. Finally, and most significantly, ΔP_3 is zero at the first antinode in figure 4-6; whereas, it is π for the cross-duct configuration.

Figure 4-7 presents propagation loss versus range for the two configurations of table 4-1. Consider first the detailed wiggly curves. These curves are the normal-mode result obtained by the coherent addition of modes 1 to 23. Modes of higher order have attenuation coefficients that exceed 0.8 dB/km and can be ignored except at very close range.
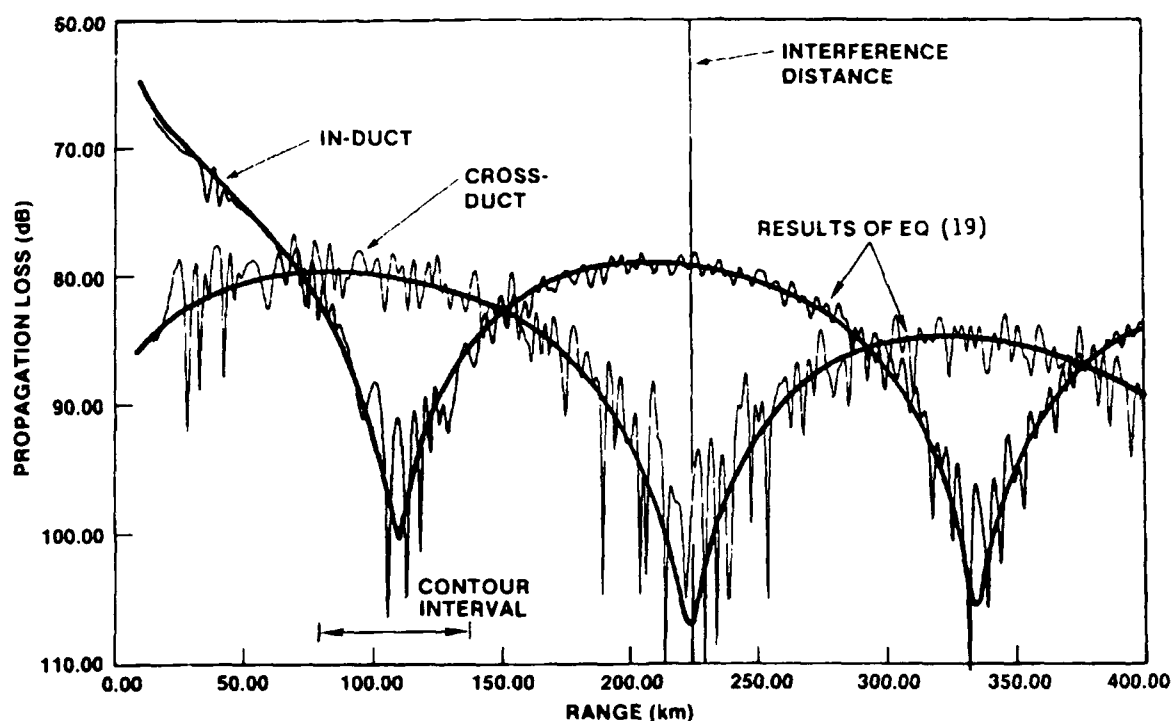
Figure 4-7. Propagation loss as a function of range for the cross-duct and in-duct configurations of table 4-1. The smooth curves represent the approximation of equation (19), based on modes 2 and 3. The detailed rapidly varying curves are the normal-mode result obtained from the coherent addition of the first 23 modes.

The heavy smooth curves in figure 4-7 are the results of equation (19) for the parameters of table 4-1. As we see, the pattern is determined by modes 2 and 3. The contribution of the other 21 modes provides a relatively minor scalloping about the smooth approximation. A range periodic transfer of energy fluctuates between the upper and lower duct. At multiples of the interference distance (including zero range), the energy is in the upper duct, with little in the lower duct. At the midranges between these multiples, the energy is in the lower duct, with little in the upper duct. The conditions

19

at multiples of the interference distance have already been covered in the discussion of equation (16). Similarly, the discussion of equation (17) covers the midrange case.

Figure 4-7 gives the results for two receiver depths. The normal-mode results for many receiver depths are now relevant and will be examined. Figure 4-8 is a contour plot of propagation loss in the range-receiver depth plane for a fixed source depth of 101.844 m. The range interval is from 80 to 140 km. This contour interval is labeled in figure 4-7 and contains the peak for cross-duct propagation and the fade for in-duct propagation. These contours are based on normal-mode evaluations at 40 receiver depths. The callouts on the right margin are the barrier depth, BD, and the depths of various nodes and antinodes of mode 3 in figure 4-6.
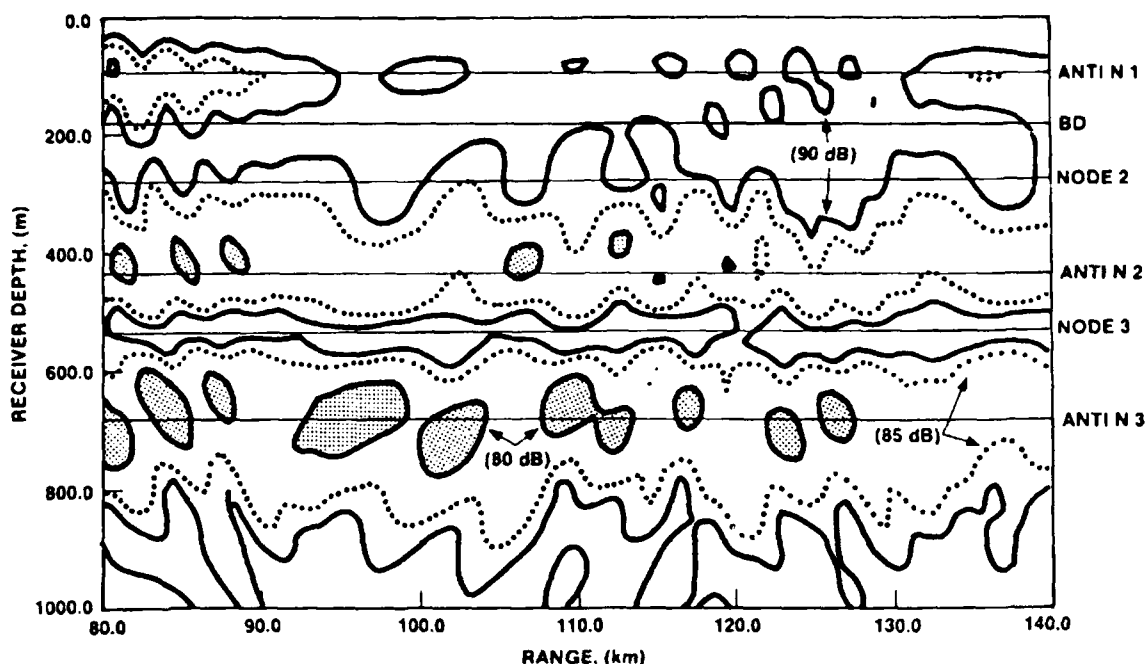
Figure 4-8. Propagation-loss contour plot corresponding to the range interval of 80 to 140 km in figure 4-7.

The shaded regions in figure 4-7 represent islands where the propagation loss is less than 80 dB. The dotted curves are the 85-dB contours. Propagation losses less than 85 dB are centered near the depths of the three antinodes of mode 3, with the largest shaded islands occurring near antinode 3. Antinode 2 is near seven shaded islands; some low-loss regions are also centered near the first antinode. These occur in figure 4-8 from 80 to 90 km and at 136 km. They occur because cancellation in the upper duct has its full effect at about 112 km and tapers off toward the minimum and maximum ranges of figure 4-8.

The solid curves in figure 4-8 are the 90-dB contours. Propagation losses greater than 90 dB occur in three general regions, with the first region above node 2. This is because modes 2 and 3 of figure 4-6 are in an out-of-phase condition for this range interval. The second region is near node 3, which is associated with the high losses for both modes 2 and 3 in figure 4-6. The third region is for receiver depths greater than about 900 m, which is associated with the depth rolloff of mode amplitude in figure 4-6 for both modes 2 and 3.

20

Thus, the contour plot of figure 4-8 illustrates that at 53.23 Hz, the acoustic field is in essence that of modes 2 and 3. The structure with range and depth clearly follows the phase relationship between these modes and the standing wave pattern of these modes as illustrated in figure 4-6.

We are now ready to consider our reference frequency of 64 Hz, chosen on the basis of figure 4-5, to have high propagation loss for a cross-duct configuration. Figure 4-9 presents propagation loss as obtained by the coherent addition of the first 27 modes. The source depth is 82.744 m for both curves, with receiver depths of 82.744 and 930.907 m, respectively, for the cross-duct and in-duct configurations. These depths are optimized for mode 6 as selected from figure 4-5. The propagation loss for the cross-duct configuration is generally more than 10 dB greater than that for the in-duct configuration. No cross-duct coupling is apparent as is illustrated in figure 4-7. Indeed, the general features can be explained by the ray diagram of figure 2-2, which is for the same source depth of 82.744 m. The in-duct propagation is dominated by low-angle propagation in the upper duct. This propagation is modulated by the contributions of the convergence zones, which are centered at range intervals of about 40 km. In figure 4-9, these bursts of modulation are labeled by their zone numbers. Note that the in-duct case of figure 4-7 also shows similar modulation at ranges near 40 and 80 km.
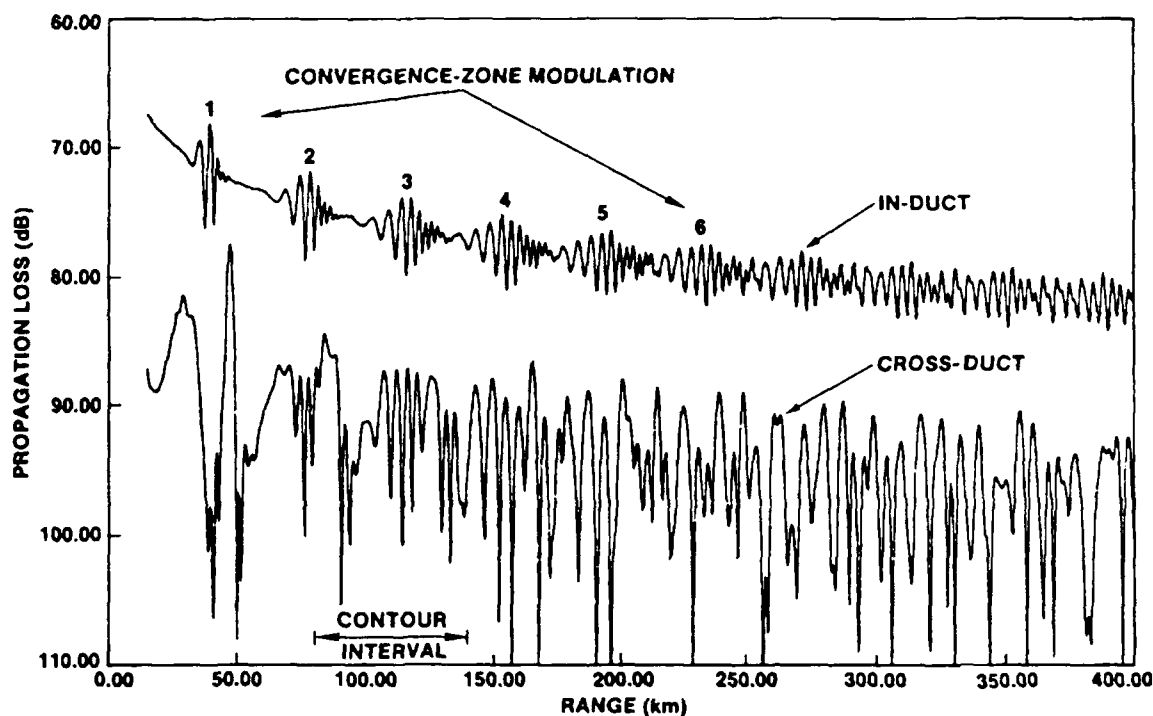
Figure 4-9. Propagation loss as a function of range for cross-duct and in-duct configurations at 64 Hz.

The nature of the cross-duct propagation is not clear-cut in figure 4-9. However, figure 4-10 clarifies it. This illustration is a contour plot over the same range interval as figure 4-8. The contour coding is also the same as for figure 4-8, with the dashed curves representing the trailing edge of the second convergence zone, and the leading and trailing edges of the third convergence zone. These curves were obtained from the ray diagram of figure 2-2, with a denser sampling of rays to establish the leading edge of zone 3. The discussion of the contours will be correlated with the ray diagram. First, we recall a general feature about contours, which can be divided into three types: (1) the major contour that threads through the entire plot; (2) islands on the outside of the major contour, for

21

which the loss is less than the contour; and (3) islands on the inside of the major contour, for which the loss is greater than the contour.
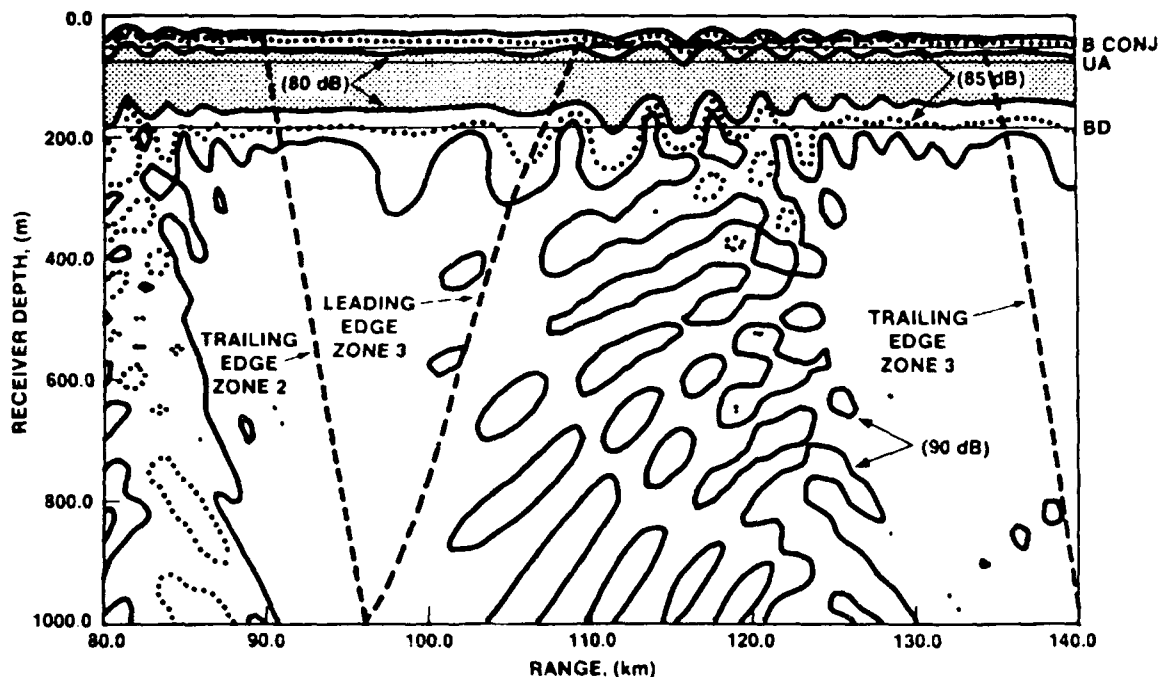
Figure 4-10. Propagation-loss contour plot corresponding to the range interval of 80 to 140 km in figure 4-9.

Two major 80-dB contours with no islands are shown in figure 4-10. The three depths called out on the right margin are the upper axis (UA), the barrier depth (BD), and the conjugate depth, where the sound speed on the upper branch of the upper duct equals that at the barrier (B CONJ). The losses less than 80 dB are generally confined about the upper axis in a band between the barrier depth and the barrier conjugate depth at 53.6 m. This represents low-angle propagation down the upper axis. The only effect the convergence zones have on the 80-dB contour is to produce some scalloping.

Consider next the 85-dB contour. The two major contours run roughly parallel to the two major 80-dB contours. However, 17 islands are below the barrier depth where the loss is less than 85 dB. Eleven of these are in the second convergence zone, and six are in the third convergence zone.

Consider the 90-dB contours. One major contour runs parallel to the upper 80-dB contour. The other major contour runs roughly parallel to the lower 80-dB contour from about 85 to 140 km. However, from 85 to 90 km, this major contour runs parallel to the trailing edge of the second convergence zone. Numerous islands with loss less than 90 dB are in the third zone. Several islands with loss greater than 90 dB are in the second zone. Note that for depths below the lower major contour for 90 dB, the loss exceeds 90 dB from about 92 to 100 km. This region represents the deepest part of the shadow zone between the second and third convergence zone.

In summary, we see no evidence of cross-duct coupling at 64 Hz. The acoustic field for receivers in the lower duct can be correlated with the convergence-zone structure formed by steep-angle rays with phase velocities that exceed the barrier sound speed.

22

We are now in a position to comment further on the work of Bucker (reference 4) cited in the introduction. Bucker used the parabolic equation method to generate propagation loss contour plots at a frequency of 53 Hz, allowing the profile of figure 2-1 to vary with range. For moderate changes with range, he found that energy was still transferred between ducts. However, the interference distance changed with range, i.e., the ranges of the peaks and nulls in the interference pattern were not uniformly spaced.

EXAMPLE OF EXTREMELY CLOSE COUPLING

Our principal concern here involves an examination of crossing C in figure 4-1. The difference in phase velocity at the frequencies of closest approach corresponding to points A and B in figure 4-1 was evaluated as 1.34 and 0.173 m/s, respectively. For comparison, we have evaluated the difference between modes 2 and 3 at 64 Hz as 0.489 m/s. In figure 4-5, we see no evidence of coupling at point A, because the difference in phase velocity at point A is more than twice that at 64 Hz (for which we saw no evidence of coupling in figure 4-9). At point A, the adjacent eigenvalues have dissimilar eigenvalues and do not resemble each other as they do at point B.

If we evaluate the mode-phase velocity for a course grid of frequencies, say at 1-Hz intervals, the curves for mode 1 and mode 2 appear to cross each other at point C. However, they do not do so. This is illustrated by figure 4-11, which presents the region near point C on a highly expanded scale. An even finer grid of frequencies has been examined, and the frequency of closest approach has been established at 92.9502 Hz, with the difference in phase velocity at this frequency being 0.0006800 m/s. As we shall see later, modes 1 and 2 strongly resemble each other, and substantial cross-duct coupling exists at this frequency. However, there is a "fly in the ointment." The evaluation of equation (18) leads to an interference distance of 34,790 km. This means that for cross-duct propagation, modes 1 and 2 will first be in phase at slightly over a 17,000-km range, which is over 40 percent of the Earth's circumference.

Before continuing the analysis of point C, we relate general features of the phase-velocity results of figures 4-4 and 4-11 to those of other investigations. The important feature is that adjacent modes never cross each other, but always veer away from each other from a point of closest approach. This effect is not unique to underwater acoustics, as we shall demonstrate by two examples of other modal phenomena.

Reference 12 discusses the mechanical vibration of plates, which involves two sets of modes. These are the thickness-shear mode and the flexural mode. Figures 6 and 7 of reference 12 show a veering away of adjacent modes. The second example is discussed on pages 153-155 of reference 13, which details the crossing of energy bands for two closely spaced energy levels of the isolated potential. The solutions for the individual levels cross each other. However, the solutions for the combined pair do not cross but steer clear of each other.

In the examples of figure 4-11 and references 12 and 13, the eigenvalues never cross each other. However, the situation is much more complicated for damped modes. Figures 32 and 33 of reference 1 present the phase velocity and mode attenuation, respectively. Two cases arise. In case 1, the phase velocities for adjacent modes do not cross, while the mode attenuation does. In case 2, the phase velocities for adjacent modes cross, while the mode attenuation remains well separated at the crossing points of the phase velocities. Figures 8 and 9 of reference 10 exhibit some very complicated interactions between a surface duct over a deep refractive duct. Both cases also arise in reference 10.
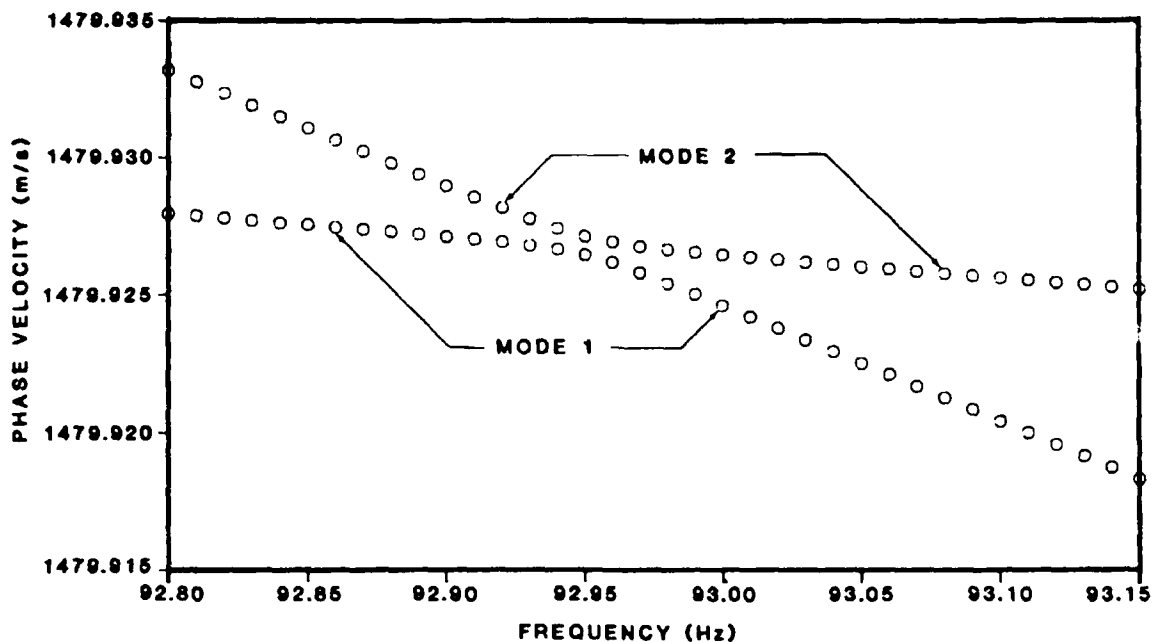
Figure 4-11. The region at point C in figure 4-1 on an expanded scale.

All of the examples of references 1 and 10 have a common feature. Whenever the phase velocities for adjacent modes come close to each other, but do not cross, the mode attenuation crosses at a nearby point. We investigated the mode attenuation at points B and C of the present article to determine if the attenuation for adjacent modes crossed. However, this could not be determined, because the attenuation is too small to yield reliable values. At points B and C, respectively, the attenuation was about 1×10^{-18} and 5×10^{-17} dB/km. At points B and C, respectively, the imaginary part of the phase velocity was 21 to 22 and 19 to 20 orders of magnitude smaller than the real part of the phase velocity. The number of significant decimal digits in the computer program is 18. Hence, the imaginary part of the phase velocity and, thus, attenuation, lie in the background noise of computer roundoff. The attenuations discussed in references 1 and 10 are well above computer roundoff, with those of reference 1 lying between 10^{-7} and 10 dB/km; and, of reference 10, lying between 10^{-1} and 10 dB/km.

We now examine the propagation loss associated with point C. Figure 4-12 presents the cross-duct coupling function for modes 1 and 2 from 60 to 100 Hz. Figure 4-12 extends the mode-2 data of figure 4-5 to 100 Hz and presents the mode-1 data, which was not addressed in figure 4-5. The narrow spike centered at about 93 Hz is the resonant peak associated with point C. The dashed curve of mode 1 is not shown over the interval from 92 to 94 Hz, because it cannot be distinguished from the solid curve of mode 2 on this scale.

The resonant peak of mode 2 in figure 4-12 has been examined with specificity. The minimum value of H_{noM} for mode 2 is 32.8727 dB and occurs at 92.9502 Hz, which is also the frequency of closest approach in figure 4-11. This minimum is 2.144 dB less than the minimum in figure 4-5 for mode 3 at 53.23 Hz. Consequently, point C leads to a slightly stronger peak than point B. The Q of this peak is 2,350, which is in marked contrast to the Q of 6.7 for the peak of mode 2 in figure 4-5.

24
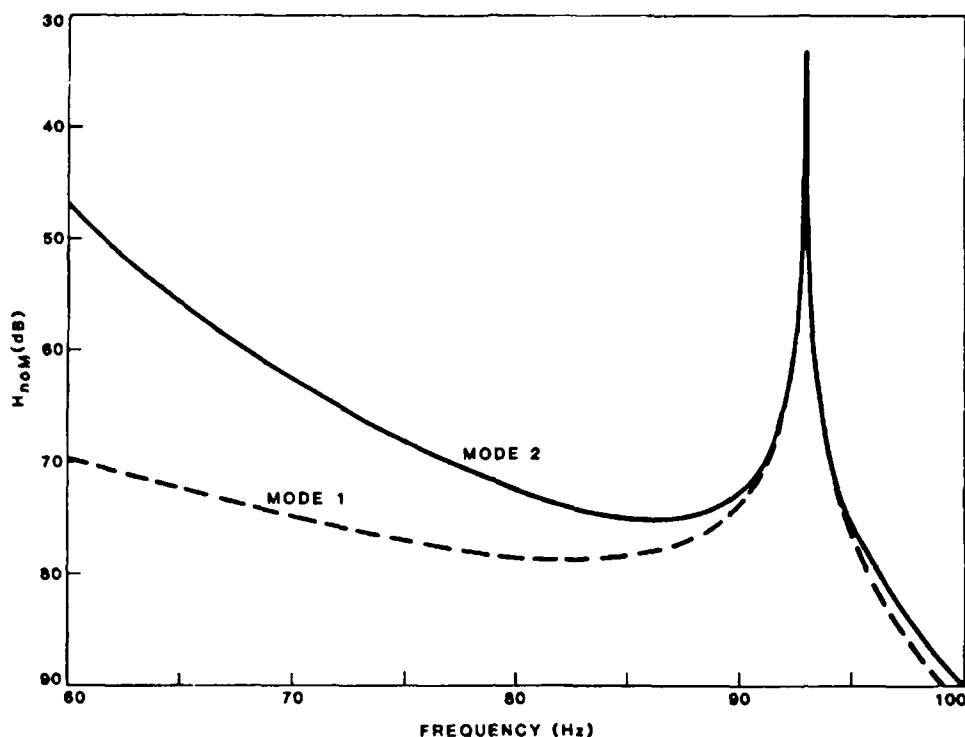
Figure 4-12. Cross-duct coupling function from 60 to 100 Hz for modes 1 and 2.

The cross-duct coupling function is slightly larger for mode 1 than mode 2. At 92.8 and 93.15 Hz, respectively, the loss is 0.059 and 0.078 dB larger for mode 1 than for mode 2, with the minimum value for mode 1 lying at the same frequency, 92.9502 Hz, as for mode 2. The smallest difference between H_{noM} for mode 1 and mode 2 is 0.0077 dB, which also occurs at 92.9502 Hz. At this frequency, the optimum source depth for mode 1 is 0.004 m deeper than for mode 2. Thus, it is clear that mode 1 and mode 2 resemble each other closely.

Figure 4-13 presents the depth functions at the critical frequency, with the solid and dashed curves referring to modes 2 and 1, respectively. The source depth is at the first antinode of mode 2 at a depth of 93.071 m, and the dashed curve for mode 1 is only shown from 180 to 360 m. For depths above and below this interval, it is indistinguishable from mode 2 on the scale of figure 4-13.

At a depth of about 265 m, the phase of mode 2 jumps from π to zero at the node. In contrast, the phase of mode 1 remains at π over the entire range of receiver depths. Thus, the valley in the mode 1 amplitude at a 265-m depth in figure 4-13 is not a true node and does not count in establishing the mode number. This valley plays the same role here that the valley plays in mode 2 at 270 m in figure 4-6.

25
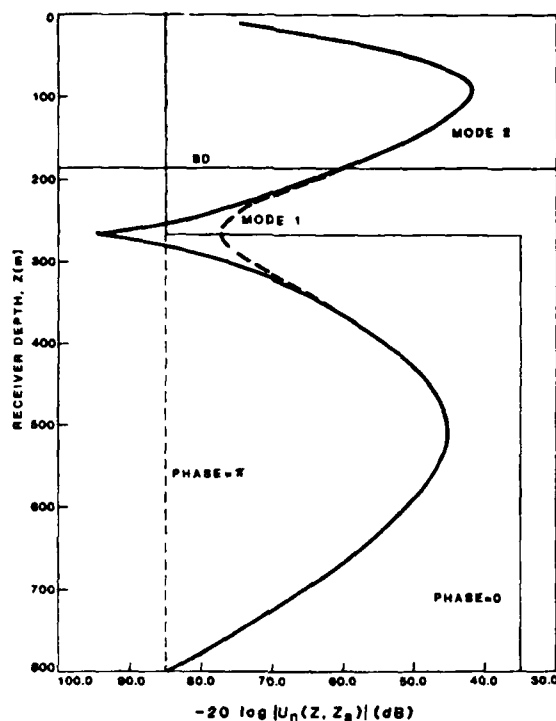
Figure 4-13. Depth function at 92.9502 Hz
for modes 1 and 2. The step function repre-
sents the phase of the depth function.

We now associate the jump in phase for mode 2 in figure 4-13 with the orthogonality property of normal modes, i.e.,

$$\int_0^\infty U_m(Z) \, U_n(Z) \, dZ = 0, \, m \neq n \ . \tag{22}$$

Thus, $U_1(Z)$ and $U_2(Z)$ cannot have the same phase over all depths, because the integrand of equation (22) would always be positive, and the integral could not be zero. Equation (22) for modes 1 and 2 is now expressed

$$\int_0^{ZN} U_1(Z)U_2(Z)dZ + \int_{ZN}^\infty U_1(Z)U_2(Z)dZ = 0 \ , \tag{23}$$

where ZN is the depth of the mode 2 node. It follows that the integrals in equation (23) must be equal and of opposite signs. Consequently, to the extent that mode 1 resembles mode 2, we may write

$$\int_0^{ZN} U_2{}^2(Z)dZ = \int_{ZN}^\infty U_2{}^2(Z)dZ \ . \tag{24}$$

Now $U_n(Z)$ and $U_n(Z_s)$ are normalized in equation (3) by D_n, which may be expressed as

$$D_n = \int_0^\infty U_n{}^2(Z)dZ \ . \tag{25}$$

D_n may be regarded as a measure of the energy content. From equation (24), note that half of the energy content of mode 2 lies above ZN. The contribution to equation 25 is relatively small between BD and ZN in figure 4-13 as compared with above BD. We conclude, then, that at the critical frequency, half the energy is associated with the upper duct and half with the lower duct. The same holds true for mode 1.

Two other features of figure 4-13 can be related to equations (24) or (25). The antinode peak in the lower duct is broader than that of the upper duct in figure 4-13. Thus, from equation (24) we correctly predict that the antinode in the upper duct is stronger than that in the lower duct. We also note in figure 4-13 that $U_1(Z)$ is larger than $U_2(Z)$ in a region about the nodal depth of mode 2. The normalization condition of equation (25) then requires that elsewhere $U_2(Z)$ be somewhat larger than $U_1(Z)$. This indicates why H_{noM} is slightly smaller (0.0077 dB) for mode 2 than for mode 1.

The same rationale as just applied to figure 4-13 can be applied to figure 4-6. Here, half the energy is contained above the node of mode 2 at a depth of about 280 m. The antinode in the upper duct is considerably stronger than in the lower duct, because the lower-duct antinodes are broader and two of them contribute significantly to the counterpart of equation (24). Furthermore, since the amplitude of mode 2 lies well above that of mode 3 at the 280-m node, the antinodes of mode 3 are stronger than for mode 2.

The examples of figures 4-6 and 4-13 suggest that at the critical frequencies, the following general conclusions apply: (1) about half of the energy content of the two modes of similar eigenvalue is associated with the upper duct and half with the lower duct; (2) the higher-order mode of the pair will have the stronger antinodes; and (3) the strength of the antinodes will be stronger in the duct which has the narrower or fewer antinodes in it.

Again, the most important feature of figure 4-13 is that modes 1 and 2 are out of phase for a receiver at the antinode in the lower duct. As previously stated, modes 1 and 2 will first be in phase at slightly over 17,000 km, which is of relatively little interest. We next determine whether modes 1 and 2 contribute significantly at zero range, where they are out of phase. The pressure amplitude of mode 1 was subtracted from that of mode 2, converted to propagation loss by equation (9). At the critical frequency (92.9502 Hz), the value was 94.0 dB; and the mode of maximum contribution is mode 9, which has a phase velocity just below that of the barrier depth. The propagation loss of equation (9) for this mode is 49.0 dB, which is not optimized for source and receiver depth. The optimized value, H_{noM}, for mode 9 is 38.4 dB, which is consistent with the values shown at 90 Hz in figure 4-7. In any case, the resonant frequency of figure 4-12 clearly plays no role in cross-duct propagation at zero range.

We next investigated the possibility that modes 1 and 2 might contribute to the propagation loss, if we detuned to some frequency slightly off resonance, so the cancellation between modes was not so severe. The phased combination of modes 1 and 2 was investigated over the resonant peak of figure 4-12, with the smallest loss over the interval measured at 93.95 dB and the largest loss at 94.18 dB. This loss seemed to increase slightly with increasing frequency. The important feature is that the resonant peak of figure 4-12 disappears completely when the amplitude of mode 1 is subtracted from that of mode 2. The rolloff of the peak in figure 4-12 is perfectly offset by a corresponding decrease in the amount of cancellation between modes. Consequently, the entire resonant peak of figure 4-12 plays no role in cross-duct propagation at zero range or indeed for ranges of practical interest. This is because the phase relationship between the modes changes so slowly with range.

The foregoing rather elegant result leads us to further examine frequencies near our other critical frequency of 53.23 Hz. (See figure 4-14 for the results.) The curve labeled even is the counterpart of the result just discussed but requires a somewhat more complicated evaluation. One cannot convert the mode 2 and 3 curves of figure 4-5 to pressure equivalents and subtract them, because the

optimum source and receiver depths are not sufficiently alike for the two modes. The procedure followed evaluated the pressure for mode 2 at the source and receiver depth which optimizes mode 3. The differences and sums of the pressures were then converted to dB and plotted in figure 4-14 as the curves labeled even and odd, respectively. The propagation loss constant of figure 4-14 represents the $H_{n+1,0} - 10\log m_0$ quantity of equation (19) for the conditions where the amplitudes are simply subtracted or added. This propagation loss may be obtained by adding 10 log r to the propagation loss constant.
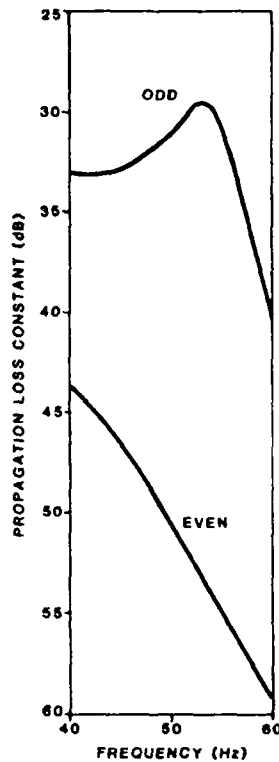
Figure 4-14. Propagation-loss constant for cross-duct propagation from 40 to 60 Hz at odd and even half-multiples of the interference distance for modes 3 and 2.

The lower curve, then, represents how the propagation loss varies with frequency at the even half-multiples of the interference distance. For example, in figure 4-7, the propagation loss, associated with modes 2 and 3, at zero range, and, at the valley, at the interference distance, can be obtained from figure 4-14 at a value of 53.23 Hz. Note that the "even" curve in figure 4-14 has a frequency rolloff similar to that of modes 4 and 5 in figure 4-5. However, the contribution of the difference of modes 3 and 2 is somewhat less than that of higher-order modes in figure 4-5. Again, the elegant feature is that the resonances subtract out, leaving a simple smooth rolloff with increasing frequency.

The upper curve of figure 4-14 represents the spectrum at odd half-multiples of the interference distance. This curve indicates how the propagation loss at the peaks of cross-duct propagation in figure 4-7 vary with frequency. A comparison of this upper curve with those of figure 4-5 indicates that the sum of modes 3 and 2 contributes more to cross-duct propagation over the band from 40 to 60 Hz than do the other normal modes. The Q of the resonant peak is about 5.5. We close this discussion by noting that the counterpart of the upper curve in figure 4-14 for point C is a curve which is 6-dB less than that of figure 4-12.

28

ANALYSIS FOR SOURCE AND RECEIVER IN THE SAME DUCT

The general objective of this discussion is to investigate the dependence of propagation on frequency when both source and receiver are in the same duct. This dependence is an important feature of propagation for double ducts. The following investigation will also help interpret the cross-duct coupling results.

Our initial interest in this topic arose from a question about point C: Is an enhancement of propagation associated with point C when both source and receiver are located in the upper duct? To answer this question, we first define the upper-duct response function, H_{nuM}, which is similar to the cross-duct coupling function. However, the receiver depth is placed in the upper duct rather than in the lower duct. Here, both source and receiver are located at the same depth, i.e., at the strongest antinode in the upper duct.

In the mode-follower program, discussed earlier in this chapter under Propagation Loss, certain antinodes are chosen as critical depths to be used as receiver depths. The source depth is one of these chosen depths. Consequently, the mode-follower program outputs H_{nuM} as well as H_{noM}. The solid curves of figure 4–15 present the upper-duct response function for modes 1 and 2 over the frequency band about point C. The result for mode 1 rapidly rolls off at lower frequencies and that for mode 2 rapidly rolls off at higher frequencies. This rolloff will be explained presently. The two curves cross each other near the critical frequency of 92.9502 Hz, with the following result. Mode 1 asymptotically approaches 23.44 dB at the higher frequencies, and mode 2 asymptotically approaches 23.46 dB at the lower frequencies.

The dashed curves of figure 4–15 are the propagation-loss constant associated with the sum of modes 1 and 2 (even) and difference between modes 2 and 1 (odd). Here, the sum corresponds to the peaks at even half-multiples of the interference distance, while the difference corresponds to the valleys at odd half-multiples. The upper dashed curve is almost a straight line of slightly positive slope which rises about 0.02 dB over the frequency interval of figure 4–15. Thus, at zero range or other even half-multiples of the interference distance, the resultant of modes 1 and 2 shows little effect of the resonant peak of figure 4–12; i.e., in-duct propagation associated with point C is not enhanced. Again note that the rapid-rolloff characteristics of modes 1 and 2 in figure 4–15 are perfect in the sense that their resultant is almost constant over the frequency interval.

Conversely, the lower dashed curve displays a marked frequency dependence for odd half multiples of the interference distance. Here, the curve goes to infinite loss at the frequency where the solid curves cross. At higher and lower frequencies, it fairs in with the solid curves as the contribution of one of the modes becomes insignificant compared with that of the other. The marked increase in loss at odd half-multiples near the critical frequency represents the following fact. The acoustic energy transmitted in the upper duct is siphoned off to form the peak in cross-duct propagation of figure 4–12.

Our next step is to introduce the lower-duct response function, $H_{n\ell M}$. Here, the source and receiver are both located at the strongest antinode in the lower duct. Since $U_n(Z)$ and $U_n(Z_s)$ are multiplicative in equation (3), one can demonstrate that

$$H_{noM} = (H_{nuM} + H_{n\ell M})/2 . \tag{26}$$

Two methods were used to generate $H_{n\ell M}$. The first and most common method was to use outputs of the mode-follower program already available for a source in the upper duct and evaluate

$$H_{n\ell M} = 2H_{noM} - H_{nuM} . \tag{27}$$

This first method poses problems when no antinode or peak is in the upper duct. The second method avoids this problem by running the mode-follower program with the strongest antinode in the lower duct as the source depth input.

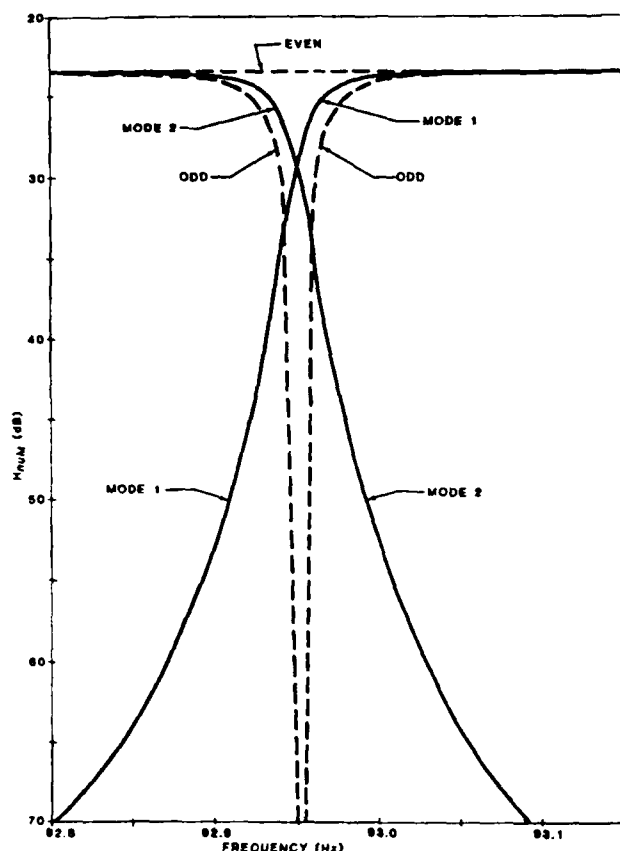Figure 4-15. Upper-duct response function from 92.8 to 93.15 Hz for modes 1 and 2. The dashed curves represent the propagation-loss constant at odd and even half-multiples of the interference distance.

The counterpart of figure 4-15 for the lower-duct response function was evaluated but is not included in this report. The behavior is very similar to that of figure 4-15. However, the roles of modes 1 and 2 are reversed, i.e., mode 1 rolls off at high frequency, while mode 2 rolls off at low frequency. The result for mode 2 asymptotically approaches 30.28 dB at higher frequencies, and that of mode 1 asymptotically approaches 30.31 dB at lower frequencies. The dashed curves of the counterpart have a similar behavior to that discussed for figure 4-15; i.e., the "even" curve again has a slightly positive slope. However, it has about 6.85-dB more loss. In figure 4-13, this corresponds to twice the difference between the loss at the lower and upper antinodes, respectively.

Note that the frequency at which modes 1 and 2 cross each other is not quite the same as the critical cross-duct frequency of figure 4-13. At the critical frequency, the amplitude at the antinodes is slightly less for mode 1 than mode 2. At the crossover frequency in figure 4-15, modes 1 and 2 have the same amplitude at the lower-duct antinode.

The solid curves of figures 4-16 and 4-17 present the upper- and lower-duct response functions, respectively, from 20 to 100 Hz for modes 1 to 4. The designators are similar to those of figure 4-5. The short vertical bars, crossing modes 3 and 4, designate the frequency for which the phase velocity of the mode equals the barrier sound speed. Letter A designates the point of closest approach for the phase velocities of modes 3 and 4. The critical frequencies near points B and C of figure 4-1 are also indicated.
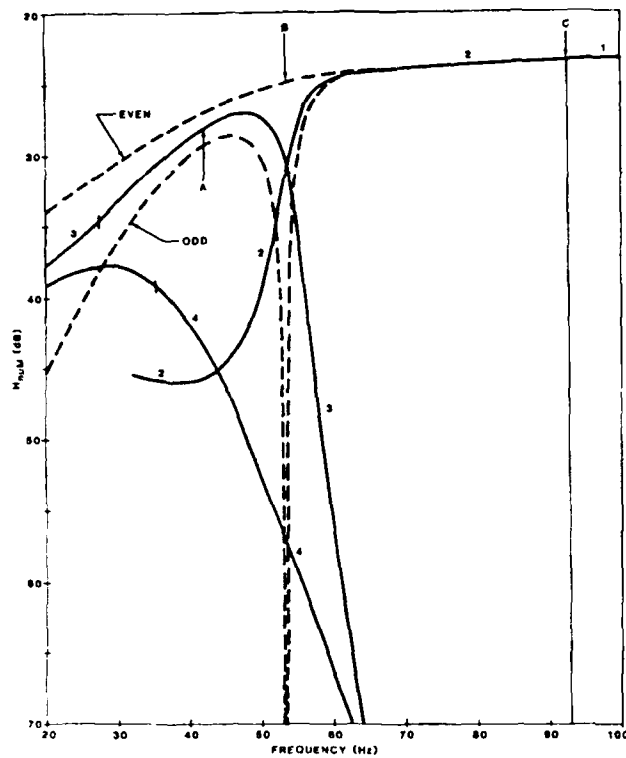
30

Figure 4-16. Upper-duct response function from 20 to 100 Hz for modes 1 and 4. The dashed curves represent the propagation-loss constant at odd and even half-multiples of the interference distance for modes 3 and 2.
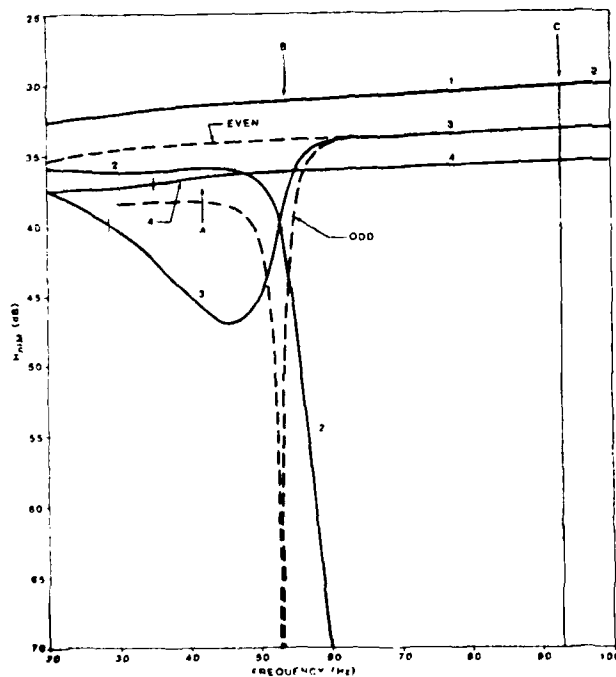

Figure 4-17. Counterpart of figure 4-16 for propagation in the lower duct.

31

The detailed structure of figure 4-15 and its counterpart collapses to vertical lines at point C in figures 4-16 and 4-17. Except for this wild behavior at point C, the results of modes 2 and 1 in figure 4-16 display an almost constant upward slope from about 70 to 1000 Hz. In figure 4-17, this constant slope extends upward from about 40 Hz. Hence, the "even" curve of figures 4-16 and 4-17 falls right into line with a trend that extends upward from 70 and 40 Hz, respectively.

Again, the frequency at which modes 2 and 3 cross each other is slightly different from the critical cross-duct frequency. At the crossover frequency in figure 4-16, modes 2 and 3 have the same amplitude at the first antinode of figure 4-6. In figure 4-17, they have the same amplitude at the third antinode of figure 4-6.

Consider the dashed curves of figures 4-16 and 4-17, which are similar to those of figure 4-15. That is, the notch formed by the solid curves is smoothly filled in by the "even" curve, the "odd" curve again goes to infinite loss at the crossover frequency, and both dashed curves fair in with the solid curve at a frequency above the critical frequency. They are different from those of figure 4-15, because they do not fair in with solid curves at the lower frequency, and the phenomena take place over a broad rather than very narrow frequency spectrum.

The dashed curves of figure 4-16 can be associated with the in-duct propagation illustrated in figure 4-7. The "even" curve represents the spectrum associated with zero range and with the first multiple of the interference distance. The "odd" curve is the spectrum associated with the valleys at the first and third half-multiples in figure 4-7. Again, the high losses for propagation in the upper duct represent energy siphoned off from the upper duct into the cross-duct peak of figure 4-14.

We evaluated the duct-response function for the single-duct counterparts of the double-duct profile. The plots will not be presented here. However, the response functions for modes 1 to 3 of the single lower duct were essentially the same as for modes 1 and 4 and the even sum of modes 2 and 3 in figure 4-17. The response functions for mode 1 of the single upper duct were essentially the same as the upper envelope of figure 4-16. We conclude that the duct response function for double ducts is quite similar to that for single ducts, provided that the crossover modes are coherently summed together.

We now demonstrate how figure 4-1 can be used to explain the major features of figure 4-16 and 4-17. In the previous discussion of figures 4-2 and 4-3, we noted that a double-duct mode had large antinode(s) in the upper or lower duct, respectively, if the eigenvalue lay close to a dashed or solid curve in figure 4-1. Thus, if an eigenvalue is associated with a dashed curve, then the loss in figure 4-16 will be small and that of figure 4-17 will be large. However if an eigenvalue is associated with a solid curve, the loss of figures 4-16 and 4-17 will be large and small, respectively.

Consider first mode 1. At frequencies below point C, mode 1 is associated with the lower duct. Mode 1 has small losses in figure 4-17, while losses in figure 4-16 exceed 70 dB for frequencies below 92.8 Hz. At frequencies above point C, mode 1 is associated with the upper duct and has low losses in figure 4-16 and high losses in figure 4-17.

The case of mode 2 is somewhat more complicated. Mode 2 is associated with the upper duct from point B to C and has low losses in figure 4-16 and high losses in figure 4-17. However, mode 2 is associated with the lower duct below point B and above point C and has high losses in figure 4-16 and low losses in figure 4-17.

At frequencies above point B, mode 3 is associated with the lower duct and has high losses in figure 4-16 and low losses in figure 4-17. At frequencies between points A and B, mode 3 is associated with the upper duct and has lower losses in figure 4-16 and higher losses in figure 4-17. At frequencies below point A, the situation is not clear-cut. Mode 3 is apparently associated with the lower

duct. As the frequency is decreased below point A, the loss in the upper duct increases in figure 4-16, while that in the lower duct decreases in figure 4-17.

Mode 4 is associated with the lower duct above point A and has high losses in figure 4-16 and low losses in figure 4-17. The situation below point A is complicated by the proximity of phase velocity to the barrier sound speed. A detailed examination of the mode 4 results of figure 4-17 indicates a slightly steeper slope between 35 and 44 Hz, which appears to be associated with the rolloff for mode 4 in figure 4-16.

The following explanation describes why the loss for a given mode is low in one duct and high in the other duct or else changing in opposite directions at transition points such as B and C. The receiver (source) depth functions are normalized by equation (25). If $U_n(Z)$ is small in one duct, then the contribution to equation (25) is small in that duct. To satisfy equation (25), the value of $U_n(Z)$ in the other duct must be large.

The cross-duct coupling function of figures 4-5 and 4-12 has high loss whenever one of the in-duct response functions has high loss. Minima in the cross-duct coupling function occur near the transition points where the in-duct response functions cross each other. At the transition point, about half the energy for the modes is associated with each of the ducts. The next discussion provides more detail on how this transition takes place.

Figures 4-18 and 4-19 present the depth function for modes 1 and 2, respectively, with two frequencies shown in each plot. One of the frequencies is chosen above point C, while the other is chosen below point C. In figures 4-7 and 4-19, the dashed and solid curves represent a strong antinode in the upper or lower duct, respectively. Dashed and solid curves are used the same as in figure 4-1. One may readily verify that the dashed curves correspond to low and high loss in figures 4-16 and 4-17, respectively. The opposite is true for the solid curves. The source depth is chosen to be near the strongest antinode. In figure 4-18, the source depth is 500 and 93.07 m for 65 and 96 Hz, respectively. Corresponding values in figure 4-19 are 93 and 500 m for 85 and 100 Hz, respectively.

Consider now how the depth function of mode 1 changes with increasing frequency. The dashed curve of figure 4-13 represents a transition from the solid curve to the dashed curve of figure 4-18. At a frequency of 65 Hz, a puny peak occurs in the upper duct and a strong antinode in the lower duct. As the frequency is increased from 65 Hz, the puny peak of figure 4-18 swells to the upper-duct peak of figure 4-13, while the strong antinode in the lower duct shrinks slightly to the lower-duct peak of figure 4-13. As the frequency is increased further to 96 Hz, the upper-duct peak of figure 4-13 rises slightly to the strong antinode of figure 4-18, while the lower-duct peak rapidly shrivels to a puny peak in the lower duct.

The behavior is just reversed for mode 2. At a frequency of 85 Hz in figure 4-19, a strong antinode occurs in the upper duct; and a weak antinode appears in the lower duct. As the frequency is increased, the strong antinode shrinks somewhat to the upper antinode of figure 4-13, while the weak antinode swells to the lower antinode. As the frequency is increased further to 100 Hz, the upper antinode shrivels to a weak antinode in figure 4-19, while the lower antinode increases slightly to the strong antinode in the lower duct.

Note that the dashed curves of figures 4-18 and 4-19 resemble each other and so do the solid curves, with one fundamental difference. In figure 4-19, a node occurs at the surface; and another node appears between the antinodes in the upper and lower ducts. However, figure 4-18 shows only a node at the ocean surface; and the minor valleys or peaks do not represent nodes or true antinodes.
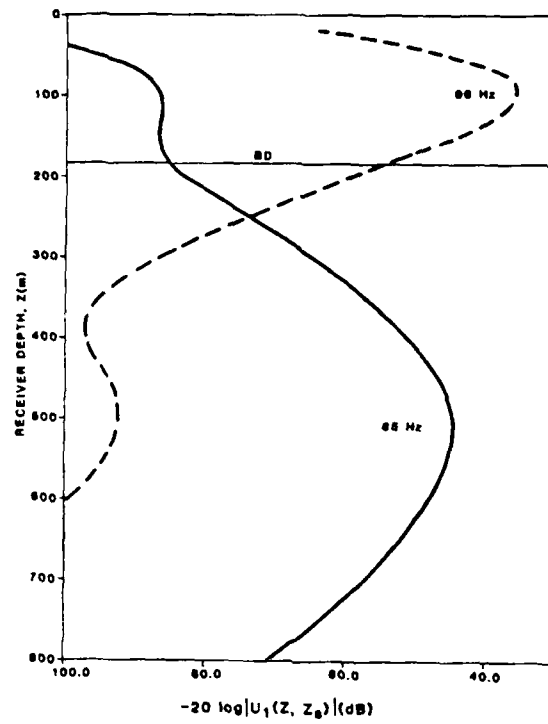
Figure 4-18. Depth function for mode 1
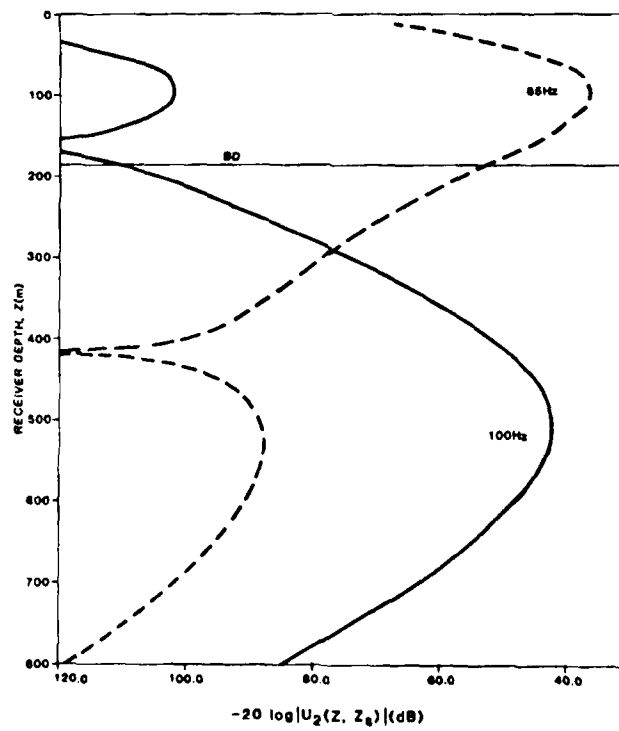at 65 and 96 Hz.

Figure 4-19. Depth function for mode 2
at 85 and 100 Hz.

34

Figure 4-20 shows the depth function for mode 2 at two frequencies which bracket point B. The source depths are 135 and 100 m for 38 and 58 Hz, respectively. At 38 Hz, two antinodes appear in the lower duct, and a slightly smaller peak exists in the upper duct. At the transition frequency of figure 4-6, the peak in the upper duct has grown larger than the two peaks in the lower duct. At 58 Hz, figure 4-20 shows a strong antinode in the upper duct and a weaker antinode in the lower duct.
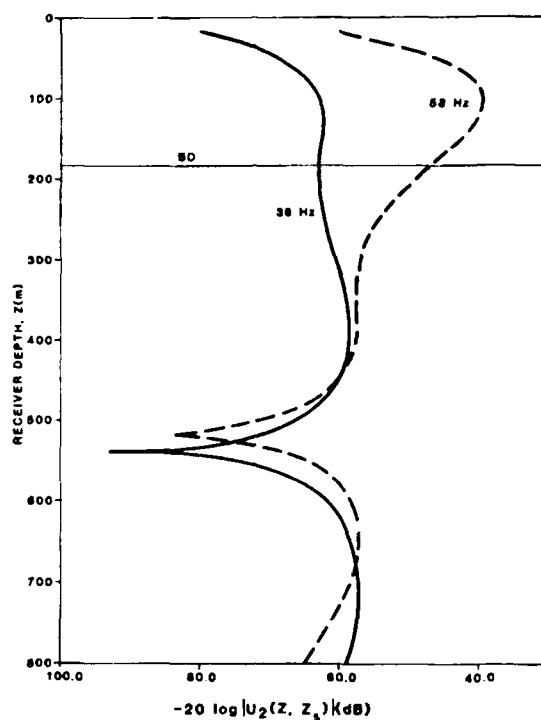

Figure 4-20. Depth function for mode 2
at 38 and 58 Hz.

Note in figures 4-5 and 4-17 that the curve for mode 2 ends abruptly at a frequency near 32 Hz. Also note the small peak and valley slightly above and below the barrier depth at 38 Hz in figure 4-20. These are spurious because they do not represent nodes or antinodes of the depth function. Such a peak and valley are well separated at the critical frequencies of points B and C. However, as the frequency is increased or decreased from the critical frequencies, these peaks and valleys decrease in amplitude and move together, and eventually disappear at a merger point. The end of mode 2 in figures 4-5 and 4-16 represents the merger point for the peak and valley at 38 Hz in figure 4-20.

This merger can be determined precisely, using the mode-follower program, as outlined in the earlier paragraph on propagation loss. The depths of the peak and the valley are determined at some frequency, such as 38 Hz. These depths are then designated as critical receiver depths. The program then steps to lower frequencies and determines the depths and propagation loss for both the peaks and valleys. (The parabolic fitting procedure works for valleys as well as for peaks, because these spurious nodes resemble parabolic sections.)

Figure 4-21 illustrates the process. The lower panel presents the mode-depth function evaluated at both peak and valley, and the upper panel presents the corresponding depth of the peak and valley. Both sets of curves merge at slightly over 32 Hz. At lower frequencies, the peak and valley have disappeared with the depth function displaying a point of inflection.

EXTREMUM DEPTH (m)

100

PEAK

150

VALLEY

200

62.1

−20 log|U₂(Z, Z₈)|(dB)

PEAK

62.2

VALLEY

62.3

62.4

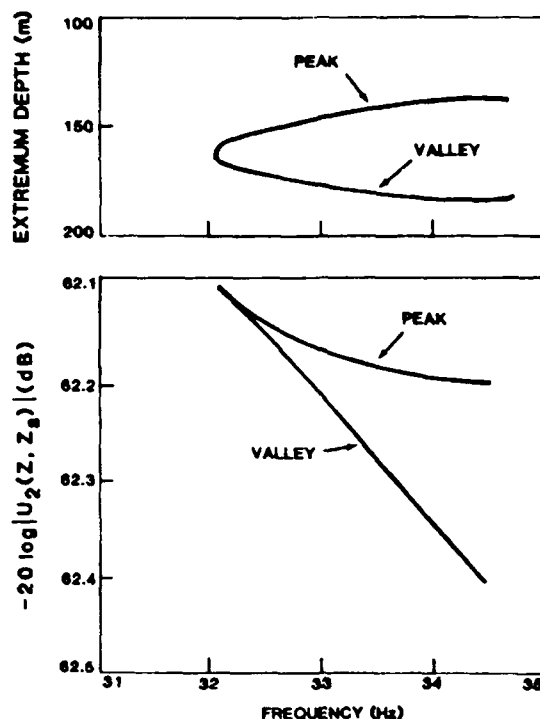62.6

31   32   33   34   35

FREQUENCY (Hz)

Figure 4-21. Plots of depth function
amplitude and depth, illustrating the
merger of the peak and valley in the
depth function of mode 2.

The exact point at which the spurious peaks and valleys disappear is not an important feature of the propagation, because the associated propagation loss is relatively high. The chief purpose of the process of figure 4-21 was to establish exactly what happens to these spurious extrema. On the high frequency side of point B, the spurious extrema merge at about 61 Hz. The 58-Hz curve of figure 4-20 shows the small peak and valley, near 375 m, just before they merge. In figure 4-5, mode 2 does not drop out at 61 Hz, because the cross-duct coupling function is evaluated at the deepest antinode and not at the one that disappears. No dropout occurs in figure 4-16 at 61 Hz, because both source and receiver are evaluated at the first antinode.

In figure 4-6, one cannot truly say that either the first or second peak (antinode) is spurious. However, the valley between is spurious. At lower frequencies, this valley merges with the first peak, forming a merger point in the upper duct. At higher frequencies, the valley moves down into the lower duct and merges with the second peak.

A similar situation occurs for the critical frequency of figure 4-13. At lower frequencies, the valley moves into the upper duct and merges with the first peak at somewhat less than 65 Hz. The solid curve of figure 4-20 still displays the peak and valley. At higher frequencies, the valley merges with the second peak at a frequency near 98 Hz. The 96-Hz curve of figure 4-18 displays the peak and valley before merger.

The frequency of merger on the high side lies closer to the critical frequency than does the frequency of merger on the low side for both modes 1 and 2. However, a higher or lower frequency may not be the determining factor. The merger on the high side is in the lower duct, while the

36

merger on the low side is in the upper duct. The rapidity of merger may depend on the duct characteristics. Further investigation of the mergers is beyond the scope of this report.

GROUP VELOCITY

This section discusses the group velocity of low-order modes and their ray-theory counterparts. The group velocities of ray theory are determined by the ratio of the cycle range over the cycle travel time as evaluated at the phase-integral result for phase velocity. The circles of figure 4-22 represent the group velocities for modes 1 to 4. The numbers indicate the modes for the double duct. These data were generated by the mode-follower program, which evaluates using the matrix method of reference 6. The dashed curve is the phase-integral result, as discussed in equations (44) to (49) of reference 5, for mode 1 of the upper duct, and will be referred to as curve 1U. Solid curves are the phase-integral result of the lower duct. The lowest and highest of these curves are for modes 1 and 3, respectively, with mode 2 falling between. They will be referred to as curves 1L, 2L, and 3L.
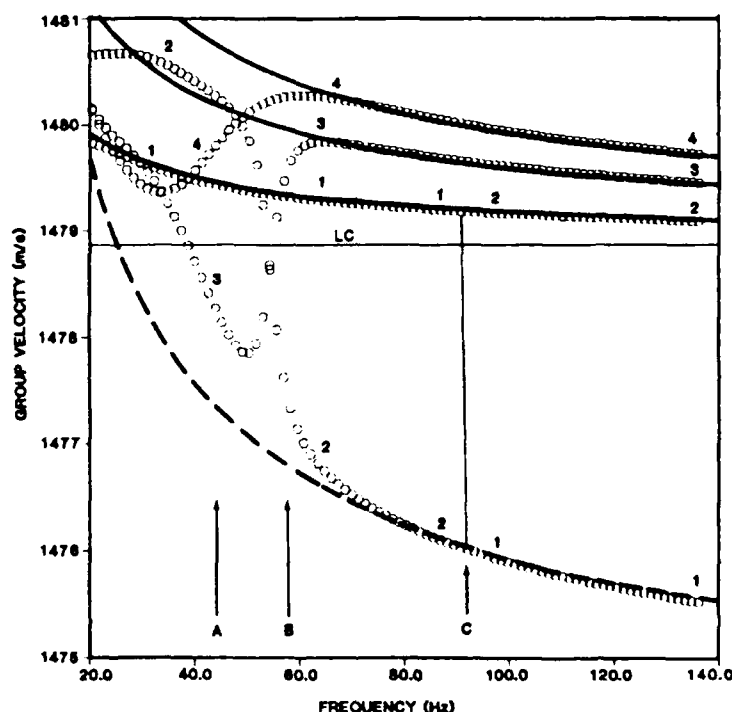
Figure 4-22. Group velocity of the first four normal modes from 20 to 140 Hz for the double duct. The curves are ray-theory approximations for single ducts.

The mode number that identifies the various discrete data of figure 4-22 is confusing. The group velocity curves of mode theory cross each other at the critical frequencies at B and C. (This is in contrast to the phase velocities as shown in figures 4-4 and 4-11, which never cross each other.) Modes 2 and 3 cross each other at point B. Figure 4-22 does not show the crossing of modes 1 and 2 at point C, because of the scale involved; however, figure 4-23 shows this crossing on an expanded scale.

The sound speed at the axis of the lower duct, called out in figure 4-22 as LC, provides a simple clue to the interpretation of the normal-mode results. This clue is that all values of group velocity less

37

than LC are associated with propagation in the upper duct, provided that the phase velocity does not exceed the barrier sound speed. The clue correlates very well with the results of figure 4–17, which represents a measure of propagation in the upper duct. At frequencies above point C, mode 1 is the dominant mode in figure 4–16 and has a group velocity well below LC in figure 4–22. Similarly, mode 2 is the dominant mode in figure 4–16 between points B and C and has a group velocity below LC in figure 4–22. Between points A and B, mode 3 is the dominant mode in figure 4–16 and has a group velocity below LC in figure 4–22. Indeed, the relative minimum in group velocity at about 48 Hz in figure 4–22 appears to correspond to the relative minimum of the upper-duct response function in figure 4–16.

Our choice of LC as a simple clue is based on ray theory. Note that the group velocities for the solid curves of figure 4–22 all lie above LC; i.e., acoustic energy in the lower duct must propagate faster than the axial sound speed of the lower duct. Thus, group velocities less than LC must be associated with propagation in the upper duct. Indeed, we could sharpen the analysis by noting that group velocities smaller than the lowest solid curve could be associated with propagation in the upper duct. This analysis suggests that the mode-4 data of figure 4–22, which lies below the mode-1 data from about 25 to 40 Hz, is associated with the upper duct. However, since the mode-phase velocity exceeds the barrier sound speed at frequencies below 35 Hz, the association is not clear-cut.

At the higher frequencies of figure 4–22, the ray-theory curves exhibit some systematic differences from mode theory. The normal-mode solution for single ducts was examined and, as was the case for the phase velocity previously discussed, these differences occurred because phase-integral solutions only approximate the mode result for single unbounded ducts. (This result is discussed in reference 5.) Figure 11 of reference 5 compares the phase-integral and normal-mode results for the single-duct formulation of the profile of figure 2–1. The modified phase-integral formulation of reference 5 brings the group velocities of ray theory into congruence with the mode results for an unbounded refractive duct. Consequently, the modified phase-integral methods will yield very good approximations to the group velocities of double ducts, except in the area of critical frequencies.

Further analysis is facilitated by the expression,

$$C_g = C_p[1 - f(dC_p/df)/C_p] \,, \tag{28}$$

which is derived in reference 5. Equation (28) expresses the group velocity in terms of the phase velocity and frequency, and applies to both mode and ray theory. Note that the group velocity depends on the slope, dC_p/df, as well as on the phase velocity, itself.

This slope term plays a fundamental role in double-duct propagation. Note that dC_p/df is in most cases negative to yield a group velocity which is smaller than the phase velocity. Therefore, a dC_p/df of larger magnitude will produce a smaller group velocity. Consider now mode 1 in figure 4–11. As the frequency is increased from 92.8 Hz, dC_p/df transitions from a smaller slope (associated with the lower duct) to a larger slope (associated with the upper duct). This slope term then causes the group velocity for mode 1 in figure 4–23 to transition from the higher group velocities of the lower duct to the lower group velocities of the upper duct.

The group velocity provides a more critical comparison between ray and mode theory than does the phase velocity because it is sensitive to dC_p/df. At low frequencies, the phase velocities of ray and mode theory look reasonably alike. However, the group velocities of ray theory look quite different from their modal counterparts.

Figure 4–24 presents group velocities for frequencies below 40 Hz. The circles represent the normal-mode results for modes 1 and 2, and the curves are phase-integral results.
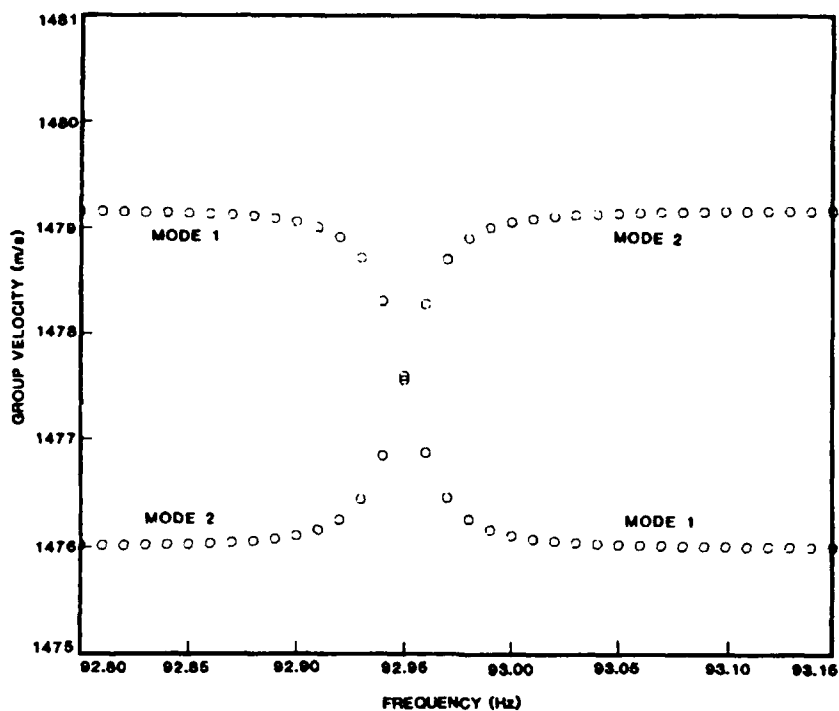
38

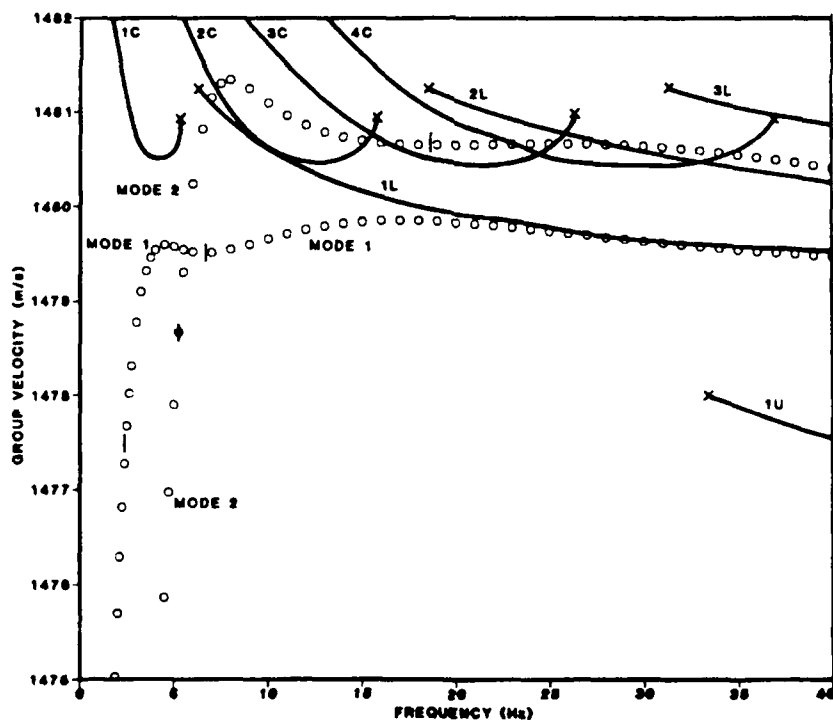Figure 4-23. The region at point C in figure 4-22 on an expanded scale.

Figure 4-24. Group velocity below 40 Hz. The curves represent ray-theory results for rays with phase velocities near the barrier sound speed. The circles are normal-mode results for modes 1 and 2.

39

Consider the phase-integral curves of figure 4-24. The curve, labeled 1U, is for mode 1 of the upper duct and is the only upper-duct result shown here, as results for higher-mode numbers fall at frequencies above 40 Hz. The curve is terminated at the upper end by an X. This and all Xs in figure 4-24 represent group velocities associated with the ray that grazes the barrier depth. The curves labeled 1L to 3L are for modes 1 to 3 of the lower duct, and the curves labeled 1C to 4C are for modes 1 to 4 of the combined ducts. These curves are associated with rays that are the convergence zone rays of figure 2-2; they have phase velocities greater than the barrier sound speed.

Consider now the group velocities of the Xs in figure 4-24. Values of R cycle for the ray that grazes the barrier depth for the upper duct, lower duct, and combined ducts are 35.5738, 4.0142, and 39.3880 km, respectively. Associated values of T cycle are 23.8811, 2.7159, and 26.5970 s, respectively. These lead to values of Cg of 1481.25, 1478.0, and 1480.92 m/s, respectively. Consider, for example, the results for $n=1$ in the phase-integral equations. The lower-duct endpoint for 1L decreases somewhat in both frequency and group velocity to the combined-duct endpoint for 1C. The upper-duct endpoint decreases significantly in frequency (from 33.5 to 5.5 Hz) and increases markedly in group velocity to the combined-duct endpoint for 1C. Similar jumps occur for higher orders of n, with the endpoints for the upper duct (for modes higher than 1) and for the lower duct (higher than 3), falling above the frequency scale of figure 4-24.

These discontinuities can be explained in terms of the analytic expressions. The phase velocity of ray theory is a continuous function. However, T cycle and R cycle are discontinuous for the grazing ray. Thus, the f that satisfies the phase-integral equation must jump to accommodate the jump in T and R cycle. The phase velocity is continuous; however, there are jumps in f and in dC_m/df.

Note that dC_g/df is a large positive value at the endpoint of the combined-duct curves. For basic ray theory, note that

$$dC_g/df = (dC_g/dC_m)(dC_m/df) .\tag{29}$$

For the grazing ray, $dR/dC_m/dC_m \rightarrow -\infty$ as C_m approaches the barrier sound speed from above. From equation (88) of reference 14, it follows that $dC_g/df \rightarrow \infty$ as C_m approaches the barrier sound speed from above. Also note that C_g forms a relative minimum for the combined-duct curves. This minimum is associated with a minimum in R cycle as a function of C_m as also can be demonstrated from equation (88) of reference 14.

Now the wave-theory results of a normal-mode approach will show no discontinuity problems in the acoustic field for phase velocities near the barrier sound speed. This occurs because the eigenvalue equation contains conditions matching the eigenfunction and their depth derivatives at the layer interfaces. The discontinuities illustrated in figure 4-24 for standard ray theory clearly pose a serious problem. This is one manifestation of a classic ray-theory problem known as the "split ray."

Murphy (reference 15) presents a modified ray theory for rays turning near a relative maximum. Murphy's study represents a place to start solving our problem, but additional work is required beyond the scope of the present report. Murphy's modified rays have two components. One is the modified reflected ray that does not penetrate the barrier, and the other is the modified transmitted ray that penetrates the barrier. Both components exist for rays with phase velocities greater than the barrier sound speed as well as less than the barrier sound speed. Murphy's approach may treat the cross-duct coupling problem as well as the problems posed at the barrier itself. The critical frequency that we observe in the modal results may be the frequency that maximizes the energy of Murphy's modified transmitted ray. A ray of this type is illustrated schematically in figure 2 of reference 15.

Consider now the normal-mode results of figure 4-24. The most distinctive feature is the relative maximum at low frequencies with a rolloff to much lower group velocities on the low frequency side.

Observe the short vertical bars intersecting the modal values on either side of the relative maximum. The bar on the low side designates the point where the mode-phase velocity equals the sound speed at 2076 m, i.e., the last interface of table 2-1. The bar on the high side designates the point where the mode phase velocity equals the barrier sound speed. For modes 1 and 2, these bars fall within 1 Hz of the end point of curves 1L and 2L, respectively.

The rapid decrease in group velocity at the lower frequencies can be attributed to the lower-boundary condition for the profile of table 2-1. Our investigation of bilinear surface ducts has revealed the following: As the phase velocity approaches the sound speed at the bottom of the duct, the imaginary part of the phase velocity begins to increase rapidly, corresponding to energy leaking out into the negative-gradient half space. This increase in imaginary part is accompanied by a more than usual increase in the mode-phase velocity as the frequency is decreased. The increase in slope of the phase velocity then reduces the group velocities, with the effect of the half space felt before the phase velocity equals the maximum sound speed.

This effect was tested by evaluating the group velocity of mode 1 for a profile in which the bottom interface was moved down to 2500 m from 2076 m. The results showed significant differences below 11 Hz and slight differences for slightly higher frequencies. Note that the largest group velocity for mode 1 in figure 4-24 lies more than 1 m/s below the largest values for mode 2. This probably results from the following. At low frequencies, mode 1 takes on the character of untrapped modes associated with the negative-gradient half space rather than the character of the modes associated with propagation in the surface duct. An example of this behavior is illustrated in figure 9a of reference 11.

Besides the effect of the negative-gradient half space, numerous other points of disagreement exist between the results of ray and mode theory. In the case of mode 2, the group velocities lie between 1481.3 and 1480.3 from 7 to 40 Hz. The ray-theory results for curves 2L and 2C lie within these same bounds, which is about the only feature of agreement between ray and mode theory. Curve 1U appears completely isolated from any modal results.

At this point, note that the profile of table 2-1 is not well suited for a low frequency analysis involving phase velocities near the barrier sound speed. The modal results at low frequency are a mishmash of at least four effects. First, the desired effect is near the barrier sound speed. Second, barrier penetration may influence the results if a point of closest approach lies near the barrier sound speed. Third, the effect of the negative-gradient half space is felt down to phase velocities below the barrier sound speed for low-order modes. Fourth, the effect of the ocean surface is felt by low-order modes associated with the upper duct.

This chapter closes with a discussion of the Airy phase. Note the relative minimum and maximum in the group velocity of mode 3 on opposite sides of point B in figure 4-22. These stationary values of group velocity are related to the Airy phase (see the subject index on page 289 of reference 9). The arrival times and approximate frequencies of major wave packets due to a transient source are associated with these stationary points. Thus, experimental verification of the coupling phenomenon of this report might best be accomplished by examining dispersion curves for a broadband source. The presence of multiple stationary values of group velocity in figures 4-22 and 4-24 will complicate the dispersion curves, but no more so than is illustrated in figure 4.33 of reference 9, which discusses a fluid layer over a semi-infinite elastic solid.

Stationary values of group velocity for mode 1 are also on opposite sides of point C in figure 4-22. However, these values are so close to the group velocities of modes 1 and 2, that for practical purposes, they are indistinguishable. The group velocity of mode 4 in figure 4-22 also has a pair of stationary values of group velocity. This appears to be related to the pair just discussed for mode 3. However, it differs in that the group velocity of mode 3 crosses near the relative minimum rather than about midway between the relative minimum and maximum.

41

Propagation in double ducts appears to be characterized by extrema in the group velocity. Tolstoy and Clay (reference 9) present several examples involving propagation in a water column overlaying a bottom structure. In figure 4-2, Jensen (reference 3) presents dispersion curves for a two-channel configuration. He notes that maxima in the group velocity correspond to modes having minimum loss, which means optimal propagation in the upper channel of his example. We tested this statement by comparing the results of figure 4-22 with those of figures 4-16 and 4-17. The frequency of minimum loss for mode 3, at about 48 Hz; and of minimum loss for mode 4, at about 29 Hz in figure 4-16, does indeed appear to be correlated with the relative minima in group velocities in figure 4-22 near these frequencies. However, the relative maxima in figure 4-22 for mode 2, near 30 Hz; and for modes 3 and 4, near 60 Hz, do not appear to have counterpart minima in the losses of figure 4-17. Perhaps the relative maxima in figure 4-22 are too broad to be associated with an obvious effect in propagation in the lower duct. In any case, the relationship between extrema in the group velocity, and optimal propagation in the associated duct, bears further study, but is beyond the scope of the present report.

5.0 PRESENT STATUS OF DOUBLE-DUCT INVESTIGATIONS

This report has presented the results of work accomplished from 1983 to 1985. We have not been content with merely turning out numerical results as exhibited in the present report, but wished to improve and simplify the theoretical approaches to facilitate understanding the mathematical and physical processes involved in duct coupling. Subsequent work has been directed at developing new theoretical approaches. The first of these new approaches is the modified phase-integral method of reference 5. The second new approach is the canonical eigenvalue method of references 16 and 17. We are currently applying this method to a double-duct configuration in which the canonical eigenvalue equation contains only two parameters. This contrasts to the standard eigenvalue approach of this report in which the phase velocity is a function of frequency and the 10-profile parameters of table 2-1. The canonical eigenvalues exhibit the characteristics of duct coupling and reduce the coupling problem to its fundamental essence.

REFERENCES

1. M. A. Pedersen and R. W. McGirr. 1982. "Use of Theoretical Controls in Underwater Acoustic Model Evaluation." NOSC TR 758. Naval Ocean Systems Center, San Diego CA.

2. D. White and D. F. Gordon. 1976. 'Analysis of Shallow Water Sound Propagation by Normal Mode Theory." *J. Acoust. Soc. Am. 60S*, 34(A).

3. F. B. Jensen. 1981. "Sound Propagation in Shallow Water: A Detailed Description of the Acoustic Field Close to Surface and Bottom." *J. Acoust. Soc. Am. 70*, pp. 1397-1406.

4. H. P. Bucker and P. W. Schey. 1984. "Sound Propagation in Range-Dependent Double Ducts." *J. Acoust. Soc. Am. 76S*, 38(A).

5. M. A. Pedersen, D. F. Gordon, and F. Hosmer. 1990. "Normal-Mode and Phase-Velocity Approaches to Phase and Group Velocities: In Simple Underwater Acoustic Ducts." NOSC TR 1331. Naval Ocean Systems Center, San Diego, CA.

6. M. Hall, D. F. Gordon, and D. White. 1983. "Improved Methods for Determining Eigenvalues in Multi-Layered Normal-Mode Problems." *J. Acoust. Soc. Am. 73*, pp. 153–162.

7. M. Hall. 1982. "Normal Mode Theory: The Role of the Branch-Line Integral in Pedersen-Gordon Type Models." *J. Acoust. Soc. Am. 72*, 1978-1988.

8. M. A. Pedersen, D. F. Gordon, and D. White. 1980. "Comparison of Ray-Theory and Normal-Mode Results for Convergence Zones." *Tenth International Congress on Acoustics*, Sydney, Australia, July 1980.

9. I. Tolstoy and C. S. Clay. 1966. *Ocean Acoustics*. McGraw-Hill, New York.

10. D. F. Gordon. 1979. "Underwater Sound Propagation-Loss Program, Computation by Normal Modes for Layered Oceans and Sediments." NOSC TR 393. Naval Ocean Systems Center, San Diego, CA.

11. M. A. Pedersen and D. F. Gordon. 1970. "Theoretical Investigation of a Double Family of Normal Modes in an Underwater Acoustic Surface Duct." *J. Acoust. Soc. Am. 47*, pp. 304-326.

12. P. C. Y. Lee and S. S. Chen. 1969. "Vibrations of Contoured and Partially Plated Contoured, Rectangular AT-Cut Quartz Plates." *J. Acoust. Soc. Am. 46*, pp. 1193-1202.

13. R. A. Smith. 1961. *Wave Mechanics of Crystalline Solids*. Chapman and Hall, London.

14. M. A. Pedersen. 1969. "Theory of the Axial Ray." *J. Acoust. Soc. Am. 45*, pp. 157-176.

15. E. L. Murphy. 1969. "Modified Ray Theory for the Two-Turning-Point Problem." *J. Acoust. Soc. Am. 47*, pp. 899-908.

16. M. A. Pedersen, D. F. Gordon, and F. Hosmer. 1990. "Canonical Eigenvalues, Part I: General Theory." NOSC TR 1332. Naval Ocean Systems Center, San Diego, CA.

17. M. A. Pedersen, D. F. Gordon, and F. Hosmer. "Canonical Eigenvalues, Part II: Application to One-Layer, Bounded Underwater-Acoustic Ducts." NOSC TR (In preparation).

REPORT DOCUMENTATION PAGE

Public reporting burden for this collection of information is estimated to average 1 hour per response, including the time for reviewing instructions, searching existing data sources, gathering and maintaining the data needed, and completing and reviewing the collection of information. Send comments regarding this burden estimate or any other aspect of this collection of information, including suggestions for reducing this burden, to Washington Headquarters Services, Directorate for Information Operations and Reports, 1215 Jefferson Davis Highway, Suite 1204, Arlington, VA 22202-4302, and to the Office of Management and Budget, Paperwork Reduction Project (0704-0188), Washington, DC 20503.

1. AGENCY USE ONLY (Leave blank)	2. REPORT DATE February 1990	3. REPORT TYPE AND DATES COVERED Final Jan 1984–May 1986

4. TITLE AND SUBTITLE

FREQUENCY SPECTRUM CHARACTERISTICS:
Underwater Acoustic Propagation in Double Ducts

5. FUNDING NUMBERS

PE: 601152N
PR: ZW09
WU: DN309 029

6. AUTHOR(S)

M. A. Pedersen, D. F. Gordon, and S. H. (Dan) Edwards

7. PERFORMING ORGANIZATION NAME(S) AND ADDRESS(ES)

Naval Ocean Systems Center
San Diego, CA 92152-5000

8. PERFORMING ORGANIZATION REPORT NUMBER

NOSC TR 1330

9. SPONSORING/MONITORING AGENCY NAME(S) AND ADDRESS(ES)

Office of the Chief of Naval Research
Arlington, VA 22217-5000

10. SPONSORING/MONITORING AGENCY REPORT NUMBER

11. SUPPLEMENTARY NOTES

12a. DISTRIBUTION/AVAILABILITY STATEMENT

Approved for public release; distribution is unlimited.

12b. DISTRIBUTION CODE

13. ABSTRACT *(Maximum 200 words)*

The characteristics of phase and group velocity and propagation loss are investigated for low-order modes with phase velocities less then the maximum sound speed separating the ducts. Cross-duct and in-duct propagation are evaluated for the source and receiver in different and identical duct(s), respectively. Detailed numerical examples are presented concerning the characteristics of the band about each critical frequency displayed. The phase-integral method of ray theory provides good first-order approximations to the mode eigenvalues, the critical frequencies, and group velocity.

14. SUBJECT TERMS

acoustics
normal modes
cross-duct propagation
in-duct propagation

15. NUMBER OF PAGES

49

16. PRICE CODE

17. SECURITY CLASSIFICATION OF REPORT	18. SECURITY CLASSIFICATION OF THIS PAGE	19. SECURITY CLASSIFICATION OF ABSTRACT	20. LIMITATION OF ABSTRACT
UNCLASSIFIED	UNCLASSIFIED	UNCLASSIFIED	SAME AS REPORT

NSN 7540-01-280-5500

Standard form 298